Journal of Radioanalytical and Nuclear Chemistry
https://doi.org/10.1007/s10967-026-11025-5

Preparation and characterisation of ^{239}Pu and ^{240}Pu thin films as sources for ^{235m}U and ^{236}U recoil ions

Lauren E. Reed[1] · Michael Block[1,2,3] · Christoph E. Düllmann[1,2,3] · Jaakko Julin[4] · Mikko Kivekäs[4] · Mikko Laitinen[4] · Andrea T. Loria Basto[1,2] · Christoph Mokry[1,2] · Iain D. Moore[4] · Andrea Raggio[4] · Dennis Renisch[1,2] · Jörg Runke[1,3] · Timo Sajavaara[4] · Jean Velten[1] · Jessica Warbinek[1,3] · Clemens Zirbes[1]

Received: 14 May 2026 / Accepted: 30 June 2026

Abstract
Recoil-ion sources of ^{239}Pu and ^{240}Pu, providing recoiling alpha-decay daughters $^{235\,m}$U and ^{236}U, were prepared by molecular plating. Comprehensive radiographic, microscopic and spectroscopic characterisation revealed thickness-dependent morphology, homogeneity, and activity distributions. Since neither recoil ion can be readily detected, ^{239}Pu sources spiked with ^{228}Th were also prepared to provide readily detectable ^{224}Ra daughter ions. Geant4 simulations, validated against ^{224}Ra surrogate measurements, reproduce recoil escape efficiencies within ~ 3%. ^{239}Pu and ^{240}Pu recoil-ion sources with thicknesses of ~ 40–55 nm produce the highest recoil rate per unit area and highest layer quality across the 24–108 nm thickness range.

Keywords Recoil-ion sources · Molecular plating · Thin film characterisation · Recoil efficiency · Actinide thin films · ^{235m}U

Introduction

Alpha-decaying radioisotopes can serve as sources for their daughter nuclides, which may emerge from sufficiently thin source layers. Such recoil-ion sources provide access to free atoms or ions of hard-to-obtain nuclides. One such example is ^{235m}U, with a half-life of 26.2(4) min [1]. The isomeric state ^{235m}U ($I^{\pi} = 1/2^{+}$) is the second-lowest known nuclear isomer, following the 8.4 eV isomeric state in ^{229m}Th [2], and is located at an excitation energy of 76.74(2) eV [3]. ^{235m}U de-excites to the ^{235}U ground state ($I^{\pi} = 7/2^{-}$) via a highly converted E3 transition, dominated by internal conversion (IC) electron emission (IC coefficient $\alpha > 10^{10}$) [4]. It is available as the α-decay daughter of ^{239}Pu ($t_{1/2} = 24\,110(30)$ a) and is populated with a total branching ratio of approximately 99.8%, enabling the use of thin ^{239}Pu layers as recoil-ion sources for the production of ^{235m}U [4].

^{235m}U and its hyperfine structure are of topical interest for collinear laser spectroscopy (CLS) at the University of Jyväskylä (JYU), Finland. Interest in these ultra-low-lying isomers, which bridge nuclear and atomic physics and are of relevance to the particle physics community, arises from the inclination to, e.g., develop nuclear clocks with the potential to outperform current atomic clocks by employing nuclear transitions rather than electron shell transitions [5]. Other studies have focused on the influence of the chemical environment on the half-life of ^{235m}U, with dependences on both its oxidation state and host material observed [6–9]. IC is energetically allowed only for electrons with binding energies below the isomer excitation energy, thereby restricting the process to outer-shell electrons. Consequently, the emitted IC electrons have exceptionally low kinetic energies, on the order of a few tens of eV (< 65 eV) [7, 10, 11]. Since the IC process depends on the electron density at the nucleus and, in the case of ^{235m}U, involves valence electrons, the half-life is not a fixed nuclear constant but varies with the chemical environment.

To enable such studies, ^{239}Pu recoil-ion sources with activities ranging from 48 to 185 kBq were prepared using molecular plating (MP) at Johannes Gutenberg University

✉ Lauren E. Reed
lreed@uni-mainz.de

1 Johannes Gutenberg-Universität Mainz, 55099 Mainz, Germany

2 Helmholtz-Institut Mainz, 55099 Mainz, Germany

3 GSI Helmholtzzentrum für Schwerionenforschung GmbH, 64291 Darmstadt, Germany

4 University of Jyväskylä, 40014 Jyväskylä, Finland

Published online: 24 July 2026

Mainz (JGU), Germany [12]. To provide ^{236}U, which has no hyperfine structure and thus is an ideal reference isotope for hyperfine structure studies, recoil-ion sources of ^{240}Pu, also an α-emitter ($t_{1/2}$ = 6561(7) a, b_α = 100%), were prepared by MP as well [13].

In the MP technique, the isotope of interest is dissolved in an organic solvent and electrodeposited onto a conductive cathode, forming a thin, uniform layer. It is an attractive method for the production of recoil-ion sources, providing a high rate of daughter isotopes [14]. High deposition yields of ≥ 90% can be achieved in a single deposition step; it is a reliable technique, and the deposited layer is generally well bonded to the backing. Since its development in the 1960s, MP has been optimised with respect to parameters such as substrate roughness, plating solvent, current density, and electrolyte concentration to produce smooth, crack-free deposits [12, 14–17].

The rate at which recoil daughter nuclides are emitted from the source and become available for CLS studies is a key performance indicator of the recoil-ion sources. It is governed by recoil escape efficiency, which depends on both MP and post-deposition conditions (e.g., substrate material and roughness, plating solvent, post-deposition drying procedure, and anode shape) and resulting source characteristics (e.g. thickness, homogeneity). These factors reflect both MP and post-deposition performance, as well as substrate properties, and their coupled optimisation is therefore essential for the development of efficient recoil-ion sources.

Direct experimental determination of the ^{235m}U recoil efficiency from ^{239}Pu sources is challenging due to difficulties in quantifying ^{235m}U de-excitation based on the low energy of the emitted IC electrons, and because of the long half-life of the ^{235}U ground state ($t_{1/2} = 7.04(1) \times 10^8$ a, b_α = 100%) [18]. Therefore, an alternative approach was employed using ^{224}Ra recoil ions emitted from ^{239}Pu sources spiked with ^{228}Th ($t_{1/2}$ = 1.913(1) a, b_α = 100%), produced by MP using identical parameters as for the pure ^{239}Pu sources [19]. The recoil energy of ^{224}Ra (96.6 keV) is comparable to that of ^{235m}U (86.2 keV), and its decay ($t_{1/2}$ = 3.6319(23) d, b_α = 100%) enables quantification via α-spectrometry, justifying its use as a surrogate in sources of similar thicknesses. [19–21].

Geant4 simulations were used to model recoil escape processes and were validated against experimentally determined ^{224}Ra recoil collection efficiencies from ^{228}Th-spiked ^{239}Pu recoil-ion sources, allowing source recoil escape efficiency determination [22–24]. The validated simulations were subsequently used to determine the ^{235m}U recoil escape efficiency for the ^{239}Pu recoil-ion sources.

Experimental ^{224}Ra recoil collection efficiency measurements were performed using the recently upgraded Detection of Internal Conversion Electrons (DICE) setup at JGU and are reported elsewhere [25]. DICE allows the collection of recoil ions in thin foils, with the additional option of subsequent low-energy IC electron counting following their emission from the collection foil during ^{235m}U de-excitation to the ^{235}U ground state, enabling accurate ^{235m}U half-life measurements [1, 25]. Previous MP studies have primarily focused on improving deposition yields, optimising deposition parameters, or characterising deposited layers using individual analytical techniques. Similarly, studies of recoil-ion sources have generally concentrated either on source preparation or on recoil collection measurements, while links between source morphology, activity distribution, and recoil escape efficiency have remained limited. A comprehensive framework that combines source preparation, multi-technique characterisation, and experimentally validated recoil ion transport modelling for actinide recoil-ion sources has, to our knowledge, not previously been reported. The proposed addition is intended solely to improve clarity by explicitly stating the gap in the existing literature and the scope of the present work. It does not modify the results, analysis, or conclusions of the manuscript. We would be grateful if this minor textual addition could be accommodated during production.

In this work, the preparation and characterisation of ^{239}Pu and ^{240}Pu recoil-ion sources by MP from N, N-dimethylformamide (DMF) are presented. Sources with varying dimensions, activities, and substrates, and at different drying conditions, were prepared. Characterisation was performed using radiographic imaging (RI), scanning electron microscopy (SEM), laser scanning microscopy (LSM), α- and γ-spectrometry, and Rutherford backscattering spectrometry (RBS). The influence of source thickness and morphology on recoil escape efficiency is evaluated, and optimised conditions for high-performance recoil-ion sources are identified. Unlike previous investigations that have typically considered source preparation, source characterisation, or recoil performance independently, the present work combines these approaches to establish relationships between source morphology, activity distribution, and recoil-source performance. Furthermore, experimentally measured ^{224}Ra recoil collection efficiencies from ^{228}Th-spiked surrogate ^{239}Pu sources are used to validate Geant4 recoil transport simulations, enabling reliable prediction of the otherwise difficult-to-determine 235mU recoil escape efficiency. This experimentally validated modelling methodology permits optimisation of recoil-ion source design and identifies recoil ion source thicknesses, areas, substrate and post-plating drying procedures that maximise recoil rate while maintaining high film quality. The proposed addition is intended solely to improve clarity by explicitly stating the gap in the existing literature and the scope of the present work. It does not modify the results, analysis, or conclusions of the manuscript. We would be grateful if this minor textual addition could be accommodated during production.

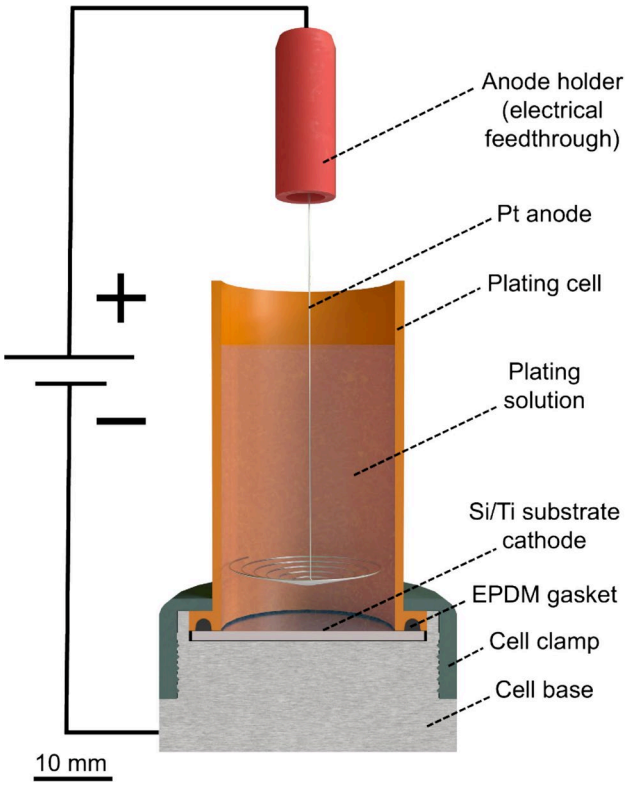

Fig. 1 Cross-sectional schematic of the molecular plating (MP) assembly, with the key components labelled, including the anode, cathode (substrate) and plating solution

Experimental

Reagents and materials

Recoil-ion sources were prepared by MP [12]. All reagents were of high-purity chemical-grade (Sigma-Aldrich). A platinum coiled-wire anode (Goodfellow, 99.99 + %, 0.5 mm diameter) was positioned centrally above a 22 or 16 mm diameter deposition aperture at the base of the plating cell (Fig. 1). The cell was constructed from Polychlorotrifluoroethylene (PCTFE) to minimise plutonium adsorption [26, 27]. Ethylene-propylene-diene monomer (EPDM) gaskets, resistant to DMF, were used to ensure chemical compatibility.

The cell was mounted on either a Si cathode substrate (Siegert wafer GmbH, single-side-polished wafer, 25 diameter, 525 µm thickness) or a Ti cathode substrate (Goodfellow, 99.9%, 25 diameter, 25 µm thickness). Prior to plating, all components were cleaned sequentially with isopropanol, acetone, and isopropanol. The anode and Ti substrates were etched in 6 M HCl for ~ 5 min, rinsed with deionised water, and then with isopropanol. Three blank platings were performed before the deposition of radioactive material to verify cleanliness.

Certification indicated that the 53-year-old ^{239}Pu stock solution consisted of plutonium oxide dissolved in dilute HCl, with an isotopic composition of > 94.84% ^{239}Pu by activity. Based on certification, the solution at the time of preparation was calculated to contain ^{241}Am and ^{240}Pu activities corresponding to ~ 1.1 and 3.3%, respectively, of the ^{239}Pu activity. The ^{228}Th certification specified that the 2-year-old stock solution consisted of thorium nitrate dissolved in dilute HNO_3, with an isotopic purity of > 99.99% ^{228}Th by activity. No characterisation data were available for the ^{240}Pu mother solution, so its activity and isotopic composition were determined by α-spectrometry of the mother solution, which showed no evidence of contaminants above the α-spectrometric sensitivity limit (~ 0.1% relative to the ^{240}Pu activity).

Before plating, aliquots of the desired source activity were evaporated to dryness and re-dissolved in 10 µL of 0.1 M HNO_3. The evaporation and redissolution steps were performed three times to prepare the final plating solutions. Final plating solutions were added to 10 mL DMF and thoroughly homogenised before transfer to the plating cell.

Source preparation

Plating solutions containing 50–210 kBq of ^{239}Pu (and additionally 2–3 kBq ^{228}Th for spiked sources) were combined in 10 mL DMF for preparation of the ^{239}Pu (and ^{228}Th-spiked ^{239}Pu) recoil-ion sources. For reference sources, 220–400 kBq of ^{240}Pu plating solution was used. The solutions were homogenised and transferred into the plating cell. Electrodeposition onto the substrate was performed for 75 min at room temperature and at a constant current density of 0.9 mA cm^{-2}. Voltages did not exceed ~ 400 V. One minute before completion, 1 mL of concentrated NH_4OH was added to prevent redissolution of the deposited layer [28]. Sources were air-dried following plating, except for a subset of ^{239}Pu sources, which were oven-dried by heating to 200 °C over 1 h, holding for 30 min, and cooling to room temperature. Aliquots of the plating solution were collected before and after deposition for subsequent α-spectrometry to determine indirect MP yields from the depletion of activity in the supernatant solution during MP. The decrease in solution activity was attributed to deposition of activity onto the cathode substrate. Direct MP yields were determined by α-spectrometry of the finished sources by comparing the measured source activity with the activity initially present in the plating solution. The unspiked and ^{228}Th-spiked sources were prepared in Jun 2021 and Jan 2025, respectively.

The ^{239}Pu and ^{240}Pu sources were prepared with systematically varied parameters to investigate their influence on layer homogeneity and recoil escape efficiency, whilst considering the experimental requirements at JYU. The varied parameters included substrate material (Si or Ti),

Table 1 Recoil-ion sources prepared by molecular plating (MP), including the main plated nuclide(s), substrate material, post-MP drying procedure, and deposition diameter. A range of plating parameters was systematically varied to assess their influence on recoil efficiency. Source IDs correspond to the nomenclature described in the text

Source ID	Main Nuclide(s)	Substrate	Post-MP Drying Method	Diameter [mm]
1,3,7,12,13,15,18,19	^{239}Pu	Si	Air	22
2a,17a	^{239}Pu	Ti[2]	Air	22
5b,9b,16b	^{239}Pu	Si	Oven[3]	22
14a,b	^{239}Pu	Ti[2]	Oven[3]	22
10,11,20,21,22	^{239}Pu	Si	Air	16
4c,8c	^{240}Pu[1]	Si	Air	22
6a,c	^{240}Pu[1]	Ti[2]	Air	22
23,24,25,26,27,28,29	^{228}Th-spiked ^{239}Pu	Si	Air	22

[1]Source IDs with suffix "*c*" denote ^{240}Pu

[2]Source IDs with suffix "*a*" denote sources deposited on Ti substrates

[3]Source IDs with suffix "*b*" denote oven-dried sources

Table 2 Alpha-particle energies and absolute intensities of the dominant lines contributing to the spectral decomposition of the ^{228}Th-spiked ^{239}Pu recoil-ion sources. Peak labels correspond to those shown in Fig. 2

Peak Assignment	Energy [keV]	Intensity [%]	Ref
$^{228}Th_1$	5340.36(15)	26.0(10)	[19]
$^{241}Am_1$	5388.25(13)	1.66(2)	[31, 32]
$^{228}Th_2$	5423.15(22)	73.4(5)	[19]
$^{241}Am_2$	5442.80(13)	13.1(3)	[32]
^{224}Ra	5448.6(12)	5.06(5)	[20]
$^{241}Am_3$	5485.56(12)	84.8(5)	[32]

post-deposition drying procedure (air- or oven-dried), plating open area diameter (16 or 22 mm), and Pu source activity (and thus layer thickness). The ^{228}Th-spiked ^{239}Pu sources were prepared with parameters matching those of the bulk ^{239}Pu sources (i.e., Si substrate, air-dried, 22 mm diameter, comparable ^{239}Pu activity range), enabling the application of the recoil escape efficiency determination methodology across all samples.

Each source was assigned a unique identifier consisting of a numerical ID and, where applicable, a suffix indicating preparation conditions where it differed from the bulk of the batch: "a" denotes Ti substrates, "b" oven-dried samples, and "c" ^{240}Pu sources. Sources without suffixes correspond to Si-based air-dried ^{239}Pu sources. This nomenclature is used throughout this work, and a full overview of all sources and preparation parameters is provided in Table 1.

Source characterisation

Sources were characterised by RI (FUJIFILM FLA 7000), SEM (Philips XL30, 20 kV), LSM (KEYENCE 3D Surface Profiler, VK-X3000) and α-spectrometry (Si PIPS

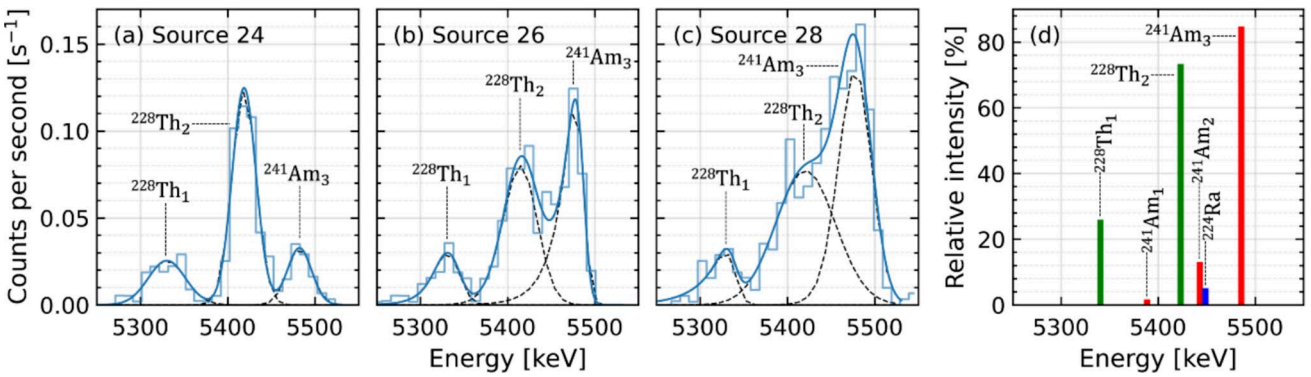

Fig. 2 Decomposed triplet structure observed in α-spectra of ^{228}Th-spiked.^{239}Pu recoil-ion sources, with increasing source thickness from (**a**)–(**c**). The measured spectra (thin solid histogram) and triplet fit (bold solid lines) are shown together with the individual peak components (dashed black lines). As the source thickness increases, the triplet becomes broader, due to increased energy straggling. (**d**) are the expected α-line positions, colour-coded by isotope, and relative intensity of the dominant transitions contributing to the multiplet in the 5.3–5.5 MeV region. The line heights correspond to intrinsic α-branching ratios and are not scaled by isotope activity or detector response. All peak and line assignments correspond to Table 2

detector, 450 mm^2 active area, 21 keV resolution). The unspiked ^{239}Pu and ^{240}Pu sources were additionally analysed by γ-spectrometry (BEGe BE3825 with integrated pre-amplifier 2002CSL, 3800 mm^2 active area, 26% relative efficiency) and RBS (1.6 MeV He^+, scattering angle 160°). For α-spectrometry, a triple alpha source (^{239}Pu, ^{241}Am and ^{244}Cm; each isotope 370(20) Bq at reference date) and a ^{241}Am source (5.0(15) kBq at reference date) were used for unspiked ^{239}Pu and ^{240}Pu sources activity calibration. For ^{228}Th-spiked source α-spectrometry, a ^{241}Am source (290(10) Bq at reference date) was used for activity calibration.

A key challenge in the analysis of the ^{228}Th-spiked sources was peak overlap in the 5.3–5.5 MeV region of the α-spectrum. The dominant α-lines contributing to this multiplet are listed in Table 2 and include two intense ^{228}Th lines (26.0% and 73.4%), three ^{241}Am lines (1.66%, 13.1%, 84.8%), and one ^{224}Ra line (5.06%). Due to the comparatively high ^{239}Pu activity, increasing counting time or reducing the detector-source distance was not feasible, as this would risk contamination and saturation.

Typical spectra exhibited a partially resolved triplet structure corresponding, in ascending energy, to the 26.0 and 73.4% ^{228}Th lines, and the 84.8% ^{241}Am line. The weaker ^{224}Ra (5.06%) and ^{241}Am (13.1%) contributions lie between the latter two peaks, while the 1.66% ^{241}Am line lies between the two ^{228}Th peaks. Figure 2d shows the expected α-line positions and relative branching ratios of the dominant transitions listed in Table 2, illustrating the intrinsic structure of the multiplet independent of detector response and isotope activity.

Accurate determination of the ^{228}Th activity is essential for subsequent recoil collection efficiency determination. To resolve the triplet, a dedicated α-spectrum analysis program was developed at JGU. The software performs background subtraction, energy calibration, and multi-peak fitting. An exponentially modified Gaussian (EMG) function was used to model peak shapes, and is given by Eq. (1):

$$f(x;A,\mu,\sigma,\tau) = \frac{A}{2\tau}\exp\left(\frac{x-\mu}{\tau}+\frac{\sigma^2}{2\tau^2}\right)\operatorname{erfc}\left[\frac{1}{\sqrt{2}}\left(\frac{x-\mu}{\sigma}+\frac{\sigma}{\tau}\right)\right] \quad (1)$$

where A is the peak area, μ is the centroid, σ is the Gaussian component standard deviation and τ is the left-sided exponential tailing parameter [29, 30]. Here, erfc(x) denotes the complementary error function,

$$\operatorname{erfc}(x) = \frac{2}{\sqrt{\pi}}\int_x^\infty e^{-t^2}\,dt \quad (2)$$

The three dominant peaks were fitted simultaneously. Figure 2 shows representative spectra of the triplet and their decomposition, with increasing source thickness from 2a to 2c. With increasing thickness, peak broadening becomes more pronounced, requiring more extensive decomposition. Minor peak contributions were estimated using the decomposed 84.8% ^{241}Am line and the well-resolved ^{224}Ra line at approximately 5685 keV (94.93%) and subtracted from the total ^{228}Th activity. To account for residual uncertainties, a conservative 20% relative uncertainty was assigned to the overlap corrections. Geant4 simulations were performed to check if any substrate backscattering corrections were needed. For the detector geometry used, no significant correction was required.

Measured α-activities were decay-corrected using certified stock solution age and isotopic composition information. Full decay-chain reconstruction was then performed to estimate contributions from unresolved daughter nuclides (e.g. from ^{240}and ^{241}Pu), β-decaying intermediates and stable end products. This approach improved both the determination of source thickness and the accuracy of ^{239}Pu activities, thereby refining the expected ^{235m}U recoil rates. RI produced grey-scale images, where pixel digital numbers were converted to per-pixel activity densities using the known total source activity. This enabled activity histograms, two-dimensional activity maps, and statistical inhomogeneity analysis. The histograms were normalised such that the total area under each distribution equalled unity, allowing comparison of activity-density distributions between sources independently of their total activity.

Absolute thicknesses of electrodeposited actinide thin layers can be difficult to determine due to limited capability for direct nanometre-scale film-thickness measurement, and incomplete knowledge of the deposited species and their densities during MP. Absolute thickness and deposited species were needed for the present study, however, so that layers of comparable thickness and material could be simulated in Geant4, since these factors influence the stopping power and thus recoil efficiency of the recoiling daughter ions in the layer. Supporting studies, including RBS, X-ray photoelectron spectroscopy and Raman spectroscopy of comparable thin films [17, 33, 34], indicate that the layers contain a mixture of oxides, hydroxides, carbonates and formates. The relative proportions of oxides and hydroxides decrease as carbonate content increases, with formate formation serving as a precursor to carbonate production [17]. In addition, comparable MP studies have shown that low potentials and locally elevated pH occur at the cathode, promoting the formation of carbonates and formates [17]. Grazing-incidence X-ray diffraction of comparable MP films further suggests that the deposited species exists in the amorphous formate phase [33]. Based on these observations, the deposited material in the present study was assumed to consist predominantly of plutonium formate ($Pu(COOH)_3$). A density of 4.0 g cm^{-3} was adopted, based on comparison with americium formate (4.8 g cm^{-3}), and its analogue,

samarium formate (3.7 g cm^{-3}) [35, 36]. Since the precise deposited species remains uncertain and may include varying proportions of oxide, hydroxide, carbonate, and formate phases, the absolute layer thicknesses derived in the present work should be interpreted as effective thicknesses under the assumed plutonium formate density. Alternative deposited compositions would primarily rescale the thickness axis through changes in density and stopping power.

For each source, RI-derived activity distributions were converted on a pixel-by-pixel basis into nuclide thickness using α-activity data, decay-chain modelling, and nuclide formate density. Total source thickness was then obtained by summing the contributions from all nuclides. Pixels with thicknesses below 0.35 nm (a conservative Pu formate monolayer estimate) were excluded as background. At this scale, the inferred thickness lies below both the minimum physically meaningful deposit thickness and the RI spatial resolution; such values are dominated by background and smearing rather than true deposition. The statistical spread of the thickness distribution was used to assign conservative uncertainties, and all uncertainties were fully propagated.

^{224}Ra and ^{235m}U recoil escape efficiency

The recoil escape efficiency of ^{224}Ra from ^{228}Th-spiked ^{239}Pu sources and of ^{235m}U from ^{239}Pu sources was determined using Geant4 simulations for a range of source thicknesses, fitted with models that were validated using experimental ^{224}Ra recoil total collection efficiencies that will be reported in [25].

For completeness, the experimentally inferred ^{224}Ra escape efficiency was also calculated, using the idea that total collection efficiency is made up of the daughter recoil escape efficiency from the source, and subsequent recoil transmission (geometric) and retention efficiencies describing the probability that an escaped recoil ion reaches the foil and then successfully implants in it, respectively. As such, using the experimentally determined total ^{224}Ra recoil collection efficiency with the simulated transmission and retention efficiencies for each source thickness, we could obtain experimentally inferred ^{224}Ra recoil escape efficiency for comparison with the model-predicted escape efficiency values at each source thickness. This would ideally validate the use of Geant4 simulation and efficiency-curve modelling for use with ^{235m}U recoils to predict the ^{235m}U escape efficiency for the unspiked sources. For both ^{224}Ra and ^{235m}U recoils,

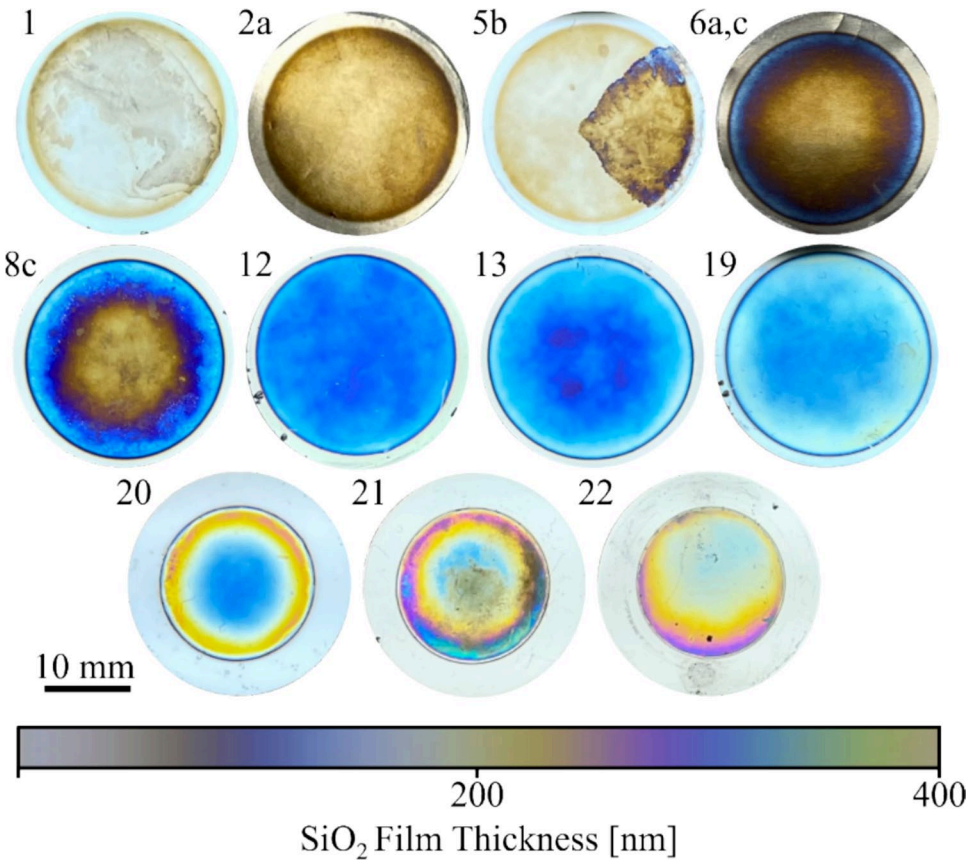

Fig. 3 Representative optical photographs of ^{239}Pu and ^{240}Pu recoil-ion sources produced by molecular plating, labelled by source ID as given in Table 1. Sources are generally arranged in order of increasing activity from left to right and top to bottom. Colour variations may reflect thickness-dependent optical interference effects. A reference colour scale for thin SiO_2 films on Si is given at the base of the figure and is adapted from [37], and serves as an example to show how the perceived colour of thin-layer changes with increasing thickness on the Si substrate at the nm scale due to light reflectance

using each source's escape efficiency, area of activity and mother activity (^{228}Th and ^{239}Pu, respectively), the recoil rate and normalised recoil rate per area could also be given.

Results and discussion

The results and discussion section is split into three parts. ^{239}Pu and ^{240}Pu recoil-ion source preparation and characterisation section presents the preparation and characterisation of the unspiked ^{239}Pu and ^{240}Pu recoil-ion sources. ^{228}Th-spiked^{239}Pu recoil-ion source preparation andcharacterisation section reports on the preparation and characterisation of the ^{228}Th-spiked ^{239}Pu recoil-ion sources. ^{224}Ra and ^{235}mU recoil escape efficiency section presents the experimentally validated recoil escape efficiency analysis and the resulting area-normalised recoil-rate trends for ^{224}Ra, ^{235m}U and ^{236}U recoils as a function of source thickness.

^{239}Pu and ^{240}Pu recoil-ion source preparation and characterisation

Imaging results

Nineteen ^{239}Pu and three ^{240}Pu recoil-ion sources were prepared by MP, giving rise to thin films with a striking variety of colours. As shown in the representative examples in Fig. 3, a trend of colour dependence on source thickness was observed. Average source thicknesses, calculated using the methodology in Source preparation, in the Experimetal section, ranged from 24 to 108 nm. At low thicknesses (~ 24–36 nm), sources predominantly appeared yellow to gold. With increasing thickness, the colour transitioned through purple and dark blue to light blue and white. At larger thicknesses, more complex colour variations were observed within individual sources. This behaviour is consistent with thin-film interference effects, in which the optical appearance varies with layer thickness, as reported for thin oxide films on silicon [37, 38]. The 16 mm sources were observed to have more colour distribution per source. Representative activity density maps shown in Fig. 4 demonstrate that spatial variations in activity density qualitatively correlate with observed colour variations, indicating that colour differences reflect variations in local thickness and, by extension, activity. Activity and thickness information per source are summarised in Table 3.

Representative histograms in Fig. 5, with their areal activity distribution centroid and full width at half maximum (FWHM) values in Table 3, and 2D thickness reconstructions in Fig. S4 (Supplementary Information) demonstrate a systematic evolution in spatial distribution with increasing thickness, dependent on the Pu isotope. The thinnest ^{239}Pu sources show relatively uniform activity distributions, with narrow, symmetric histograms centred at ~ 300–400 Bq mm^{-2}, consistent with homogeneous thin films. At intermediate thicknesses (~ 48–89 nm), these distributions begin to broaden and become increasingly skewed. While coverage remains fairly uniform, some localised regions of activity accumulation begin to develop, suggesting the onset of non-uniform growth. For thicker sources (> 90 nm), activity maps show more pronounced spatial variation, particularly at the edges of the plated area, and the histograms become broader and more asymmetric, indicating greater variability in local thickness. They exhibit the largest spatial heterogeneity,

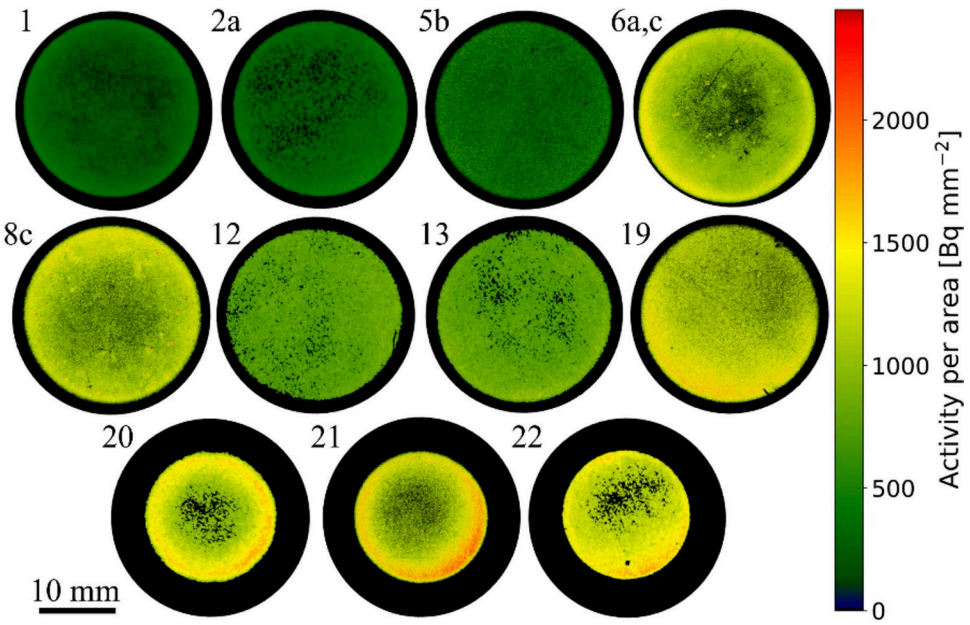

Fig. 4 Radiographic activity density maps of representative ^{239}Pu and.^{240}Pu recoil-ion sources, labelled by source ID as given in Table 1

Table 3 Thickness, active area, Pu and ^{241}Am activity, and activity density histogram centroid and full width at half maximum (FWHM) values for ^{239}Pu and ^{240}Pu recoil-ion sources produced by molecular plating. Source ID as given in Table 1

Source ID	Thickness [nm]	Area [mm^2]	Pu Activity [kBq]	^{241}Am Activity [kBq]	Centroid Activity [Bq mm^{-2}]	FWHM [Bq mm^{-2}]
1	24.0(16)	346(14)	48(3)	0.51(4)	290(30)	125(3)
2a	25.3(17)	350(14)	52(4)	0.55(4)	300(30)	110(3)
3	29.8(20)	320(13)	55(4)	0.59(4)	360(30)	261(3)
4c	28.2(17)	350(14)	213(13)	–	610(40)	273.7(24)
5b	35.8(24)	336(13)	70(5)	0.74(5)	430(30)	265(3)
6a,c	48(3)	355(14)	367(21)	–	1040(50)	407(4)
7	50(3)	339(14)	99(7)	1.07(7)	600(40)	310(3)
8c	50(3)	361(14)	392(23)	–	1090(50)	449(5)
9b	51(3)	342(14)	101(7)	1.08(7)	610(40)	355(3)
10	61(4)	197(8)	70(5)	0.74(5)	730(50)	480(6)
11	64(4)	185(7)	69(5)	0.73(5)	770(60)	308(5)
12	64(4)	360(14)	134(9)	1.42(10)	770(40)	153.3(9)
13	65(4)	362(14)	137(9)	1.46(10)	780(40)	158.5(18)
14a,b	68(5)	360(14)	142(10)	1.51(10)	810(40)	189.8(19)
15	78(5)	340(14)	153(10)	1.63(11)	930(50)	568(7)
16b	83(6)	358(14)	172(12)	1.83(12)	990(50)	435.0(18)
17a	89(7)	358(14)	185(14)	1.97(15)	1060(50)	277(5)
18	97(7)	350(14)	197(14)	2.10(14)	1160(50)	605(9)
19	100(7)	356(14)	206(14)	2.19(15)	1190(50)	497(3)
20	105(7)	202(8)	123(9)	1.3(9)	1260(70)	671(3)
21	107(5)	196(8)	121(6)	1.3(7)	1280(70)	741(12)
22	108(7)	189(8)	119(8)	1.3(9)	1290(70)	404(6)

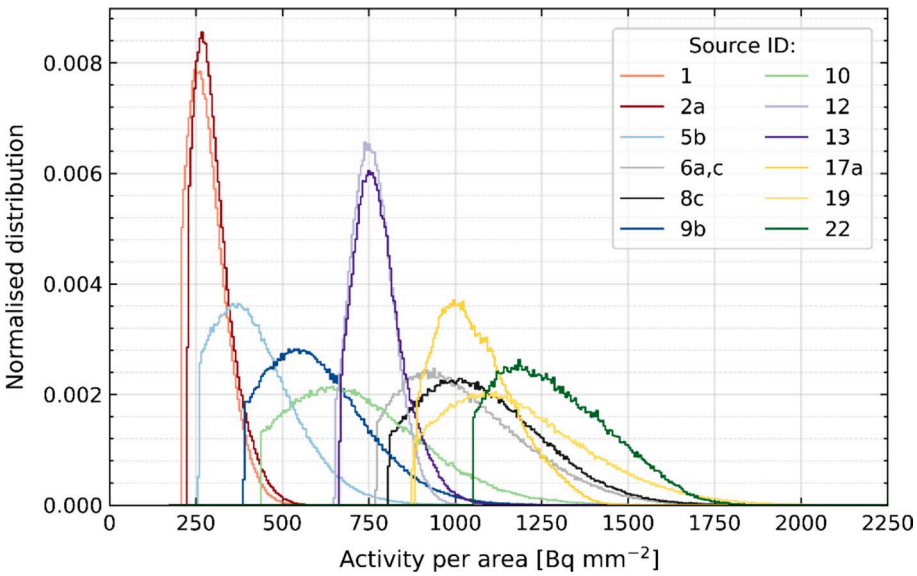

Fig. 5 Representative activity density histograms derived from radiographic imaging of ^{239}Pu and.^{240}Pu recoil-ion sources, with legend source ID as given in Table 1. Histograms were normalised such that the total area under each distribution equals unity. Homogeneous sources have sharper, more symmetric, and well-defined peaks. Centroid and full width at half maximum (FWHM) values are listed in Table 3

with localised regions of elevated activity density. These features are consistent with material accumulation at the edges of the plated area, resembling a "coffee-ring" effect, likely arising during solvent evaporation, in which, during drying of thicker sources, particles migrate to the edges of the deposition due to the Marangoni effect [39]. The ^{240}Pu sources, ranging from 28 to 50 nm in thickness, showed similar trends, and their distribution metrics were more consistent with those of end-intermediate-to-thicker-range ^{239}Pu sources, owing to their higher activity. 16 mm ^{239}Pu

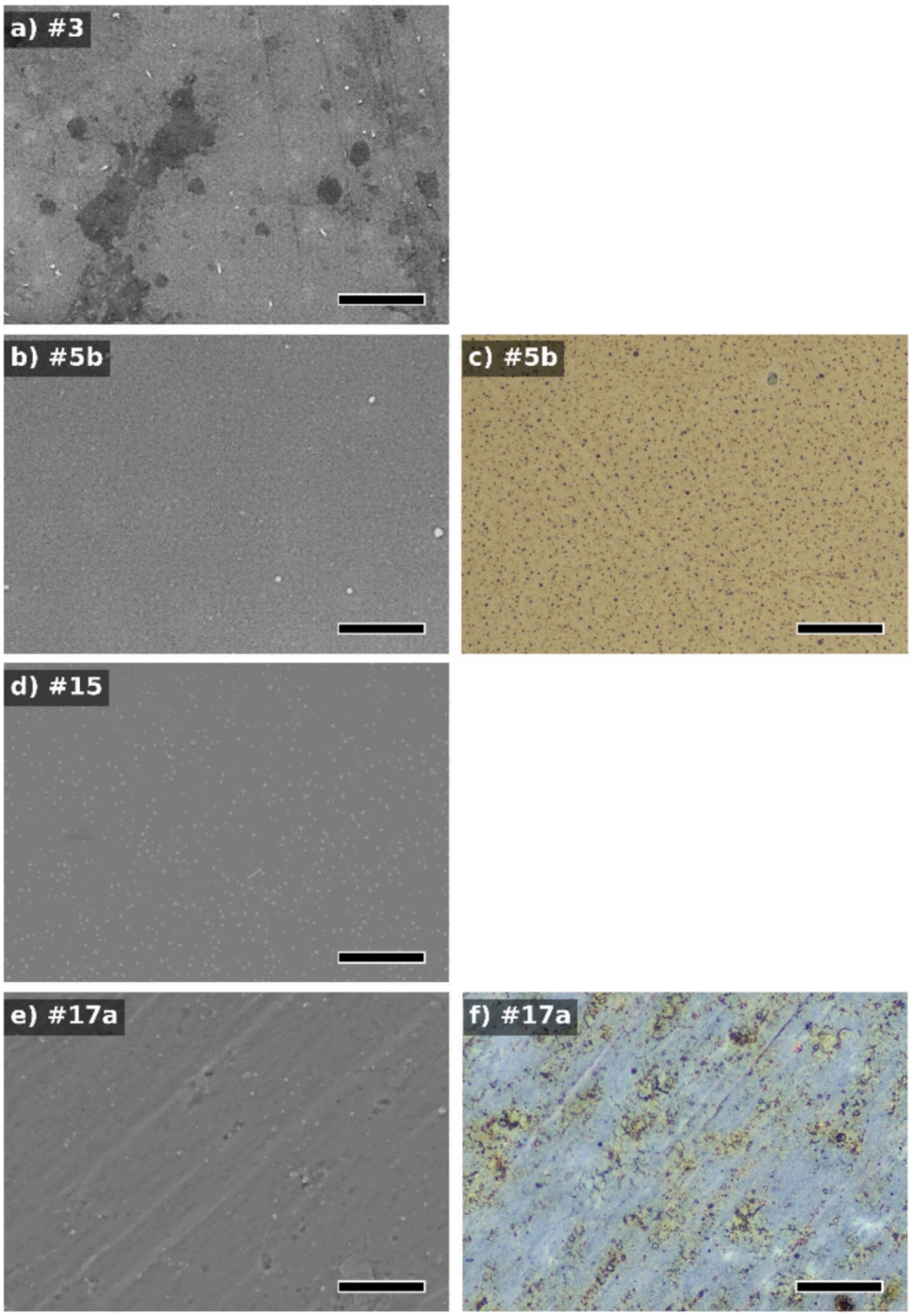

Fig. 6 Scanning electron microscopy (SEM) secondary electron (left) and laser scanning microscopy (LSM) (right, where available) images of representative ^{239}Pu recoil-ion sources, labelled by source ID as given in Table 1, from thinnest (top row) to thickest (bottom row). Scale bar: 20 µm

sources showed the "coffee-ring" effect more prominently and showed, on average, the broadest activity distributions.

Overall, results show a clear transition from uniform thin films to increasingly heterogeneous layers as source thickness increases. No systematic dependence of the activity distribution on the substrate material or post-deposition drying conditions was observed. Using the dispersion and distribution metrics, the sources were ranked from most to least homogeneous, and the most laterally uniform films were observed to be sources 1, 2a, 12, 13, and 14a,b, with the least uniform being the thickest sources, especially sources 20 and 21. Figures showing all nineteen plutonium sources and their full analysis are provided in Figs. S1 – S4 of the Supplementary Information.

SEM imaging shows that sources with thicknesses below 89 nm exhibit smooth, continuous, and largely crack-free surfaces. LSM is in good qualitative agreement with these observations and provides additional contrast for features

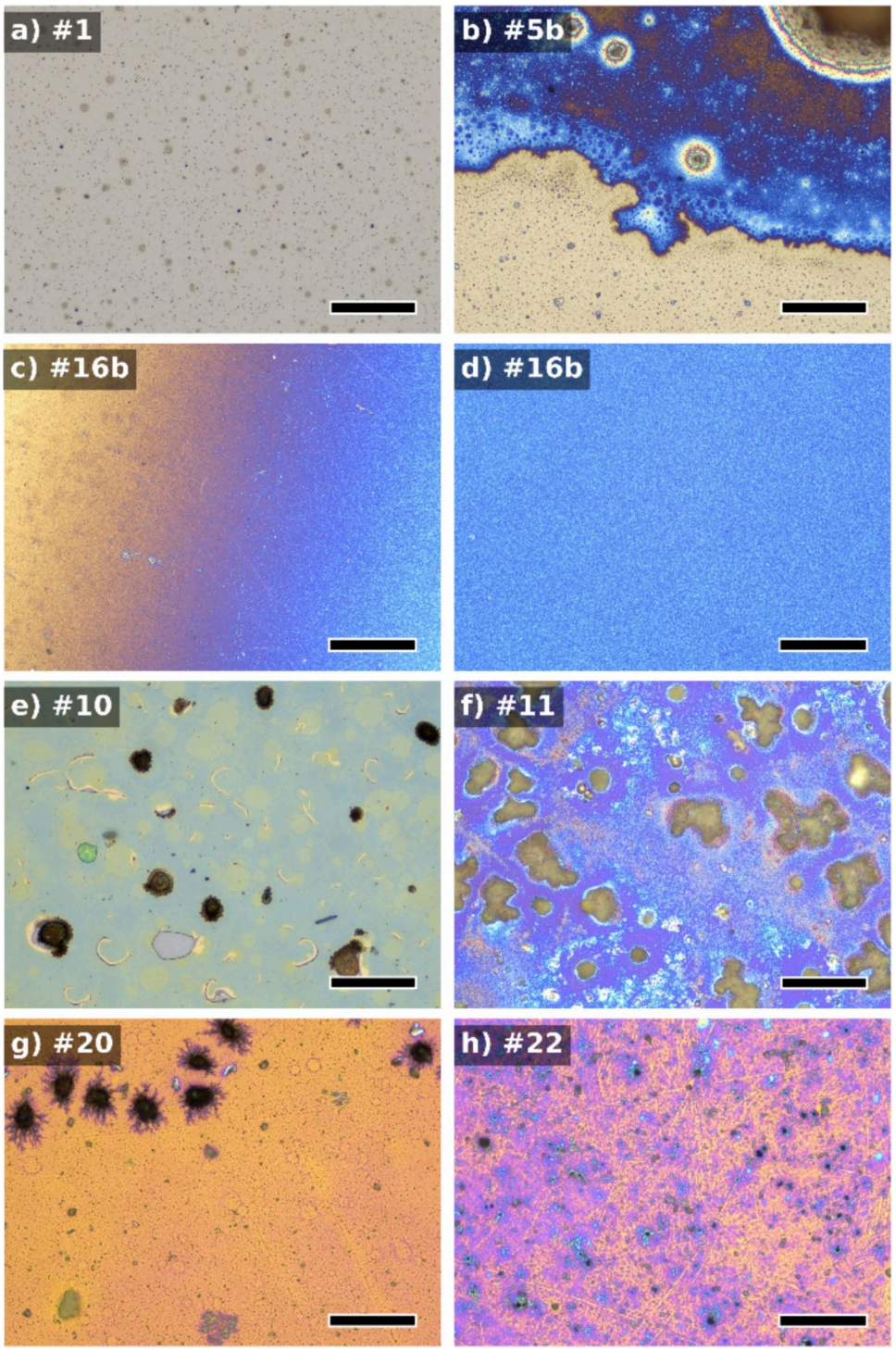

Fig. 7 Laser scanning microscopy (LSM) images in optical mode (coaxial illumination) of representative ^{239}Pu and ^{240}Pu recoil-ion sources taken ~ 5 y after preparation, labelled by source ID as seen in Table 1. Panels show selected regions illustrating thickness-dependent morphology and defect structures: (**a**) centre; (**b**, **e**–**h**) defect regions; (**c**–**d**) edge-to-centre. Scale bar: 40 µm. Additional images provided in Fig. S5, Supplementary Information

not readily resolved by SEM secondary electron imaging. Representative paired images are shown in Fig. 6.

LSM reveals a complex, thickness-dependent morphology consistent with classical thin-film growth behaviour [40]. Results reflect the combined influence of film formation during deposition, post-deposition treatment, and long-term evolution (~ 5 y). No single mechanism fully explains the morphology; rather, it is the result of superimposed growth, restructuring, and defect evolution processes.

A clear morphological progression is observed as thickness increases. For thin layers (~ 24–30 nm), surfaces are largely uniform and continuous, characterised by a fine, dense speckled texture with minimal large-scale features

(Fig. 7a). Oven-dried samples in the range ~ 36–51 nm retain a broadly similar morphology (Fig. 6c), however localised regions exhibit clustering and the emergence of circular and partially coalesced domains, forming ring-, sponge- and bubble-like structures (Fig. 7b). Localised film peeling and boundary-type features are also observed. These features are not present in non-oven-dried samples of comparable thickness, indicating that thermal treatment promotes the growth and coalescence of local inhomogeneities. At intermediate thicknesses (~ 50–89 nm), the films exhibit the highest degree of lateral uniformity. Surfaces are characterised by densely packed fine grains with minimal large-scale inhomogeneity, particularly in central regions (Fig. 7c–d). At larger thicknesses (up to 108 nm), all available LSM sources were 16 mm in diameter. All 16 mm diameter sources consistently exhibit poorer morphological quality than 22 mm sources and have thus far been excluded from the analysis. These smaller sources show more pronounced large-scale inhomogeneities and complex pattern formations. Complex pattern formation and inhomogeneities observed included evidence of bubbles and blisters (Fig. 7e–f), linear marks (Fig. 7g–h), branched and star-like structures (Fig. 7e, g), and circular domains (Fig. 7g).

A range of blister-like features was observed, including spherical bubbles, subsurface and surface blisters, ruptured (C- and O-shaped) features exposing the substrate, and coalesced blister structures. The fine-speckled morphology of otherwise homogeneous films may also indicate gas-related processes. While the exact origin cannot be unambiguously determined, these features are consistent with H_2 blistering reported in thin films on Si and glass substrates exposed to hydrogen [40–44]. H^+ is considered the most likely species responsible, as electrodeposition conditions promote H_2 evolution at the cathode [17]. The observed micron-scale features are consistent with H_2-induced blistering, whereas He generated by self-irradiation would be expected to produce primarily nanoscale features. The larger blister sizes following oven drying also align with H_2-induced effects reported in the literature [44–48].

Such blister formation is typically associated with gas accumulation at defect sites, such as inclusion–matrix interfaces, impurities, oxide particles, and pre-existing voids, and leads to delamination, surface bulging, and stress-driven cracking [45, 49, 50]. The absence of comparable blistering in Ti-supported sources (Fig. 6f) is consistent with the literature, which states that substrate choice is particularly important [41].

Such high-quality optical photographs of electroplated plutonium thin films have not been published to date. The present data show a wide range of colours, patterns, and morphological features. Additional examples are provided in Fig. S5 of the Supplementary Information.

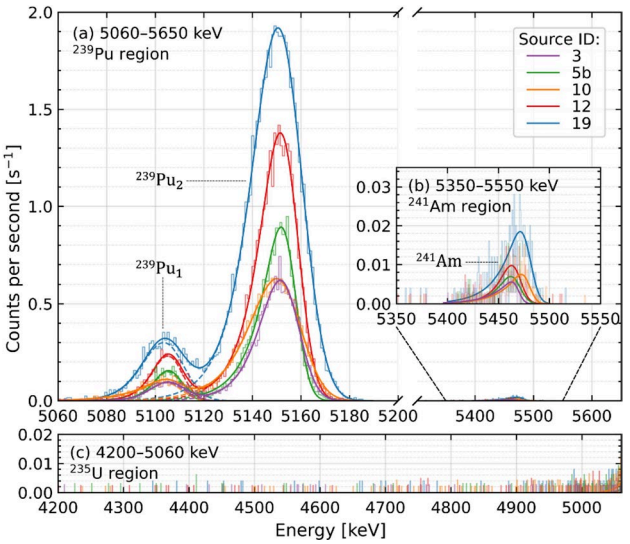

Fig. 8 Alpha-particle spectra of representative ^{239}Pu recoil-ion sources. Measured spectra (solid histogram), total peak fits (bold solid), and individual peak components (dashed) are shown. (**b**) is a magnified inset of (**a**) ^{241}Am region. (**c**) shows the ^{235}U region, demonstrating the absence of detectable daughter activity

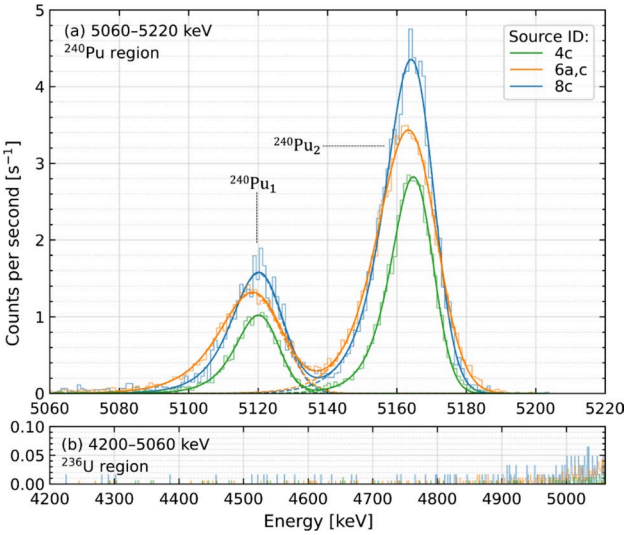

Fig. 9 Alpha-particle spectra of the ^{240}Pu recoil-ion sources. Measured spectra (solid), total peak fits (bold solid), and individual peak components (dashed) are shown. (**b**) shows the ^{236}U region, indicating the absence of detectable daughter activity

Alpha-spectrometry results

Alpha-particle spectrometry confirmed that the ^{239}Pu and ^{240}Pu sources contained 48–123 kBq and 213–392 kBq, respectively. Activity and isotopic composition determined by α-spectrometry are summarised in Table S1 (Supplementary Information). The average direct MP yield, determined from measured source activities, was 94(3)%, while the

average indirect yield, determined from depletion of activity in the plating solution, was 97(2)%. This consistently high deposition efficiency across all plated isotopes indicated that MP was highly effective for producing ^{239}Pu and ^{240}Pu recoil-ion sources. Representative α-spectra for ^{239}Pu and ^{240}Pu sources are shown in Figs. 8 and 9, respectively. All sources of a given isotope exhibited comparable spectral quality, with peak fits yielding coefficients of $R^2 \geq 0.95$. Overall, the measured peak energies, FWHM, and intensities provided in Table S1 (Supplementary Information) are consistent with literature values within uncertainties, confirming the reliability of the peak decomposition and subsequent analysis.

For the ^{239}Pu sources, the two dominant α-lines at 5144 keV and 5157 keV could not be resolved due to intrinsic detector-resolution limitations, despite the large source-to-detector distance used to avoid contamination and saturation effects and to improve resolution [4]. Similarly, the three dominant ^{241}Am α-lines at 5388 keV, 5443 keV, and 5486 keV were not fully resolved and were therefore treated as a combined contribution in the fitting procedure [32]. The corresponding peak fit represented the combined sum of these unresolved components. The measured ^{241}Am-to-^{239}Pu activity ratio was 1.07(1)%, consistent across all sources. The total measured ^{241}Am activity differed from the decay-chain-reconstructed values by approximately 3%, indicating good agreement between independent activity determinations. No additional α-lines attributable to impurities were observed in either source batch. No detectable activity was observed at the characteristic α-energies of recoil daughters (e.g. ^{235}U at 4365 keV and 4396 keV and ^{236}U at 4445 keV and 4494 keV), in accordance with their long half-lives and correspondingly low activities [18, 51]. This highlights the difficulty of direct recoil efficiency determination using α-spectrometry for such sources.

Gamma-spectrometry results

Gamma-ray spectrometry was performed on representative ^{239}Pu and ^{240}Pu recoil-ion sources to verify isotopic composition and to check for impurities. Representative spectra are shown in Figs. 10 and 11. Peak assignments, energies, and FWHM values for all identified γ-transitions are provided in

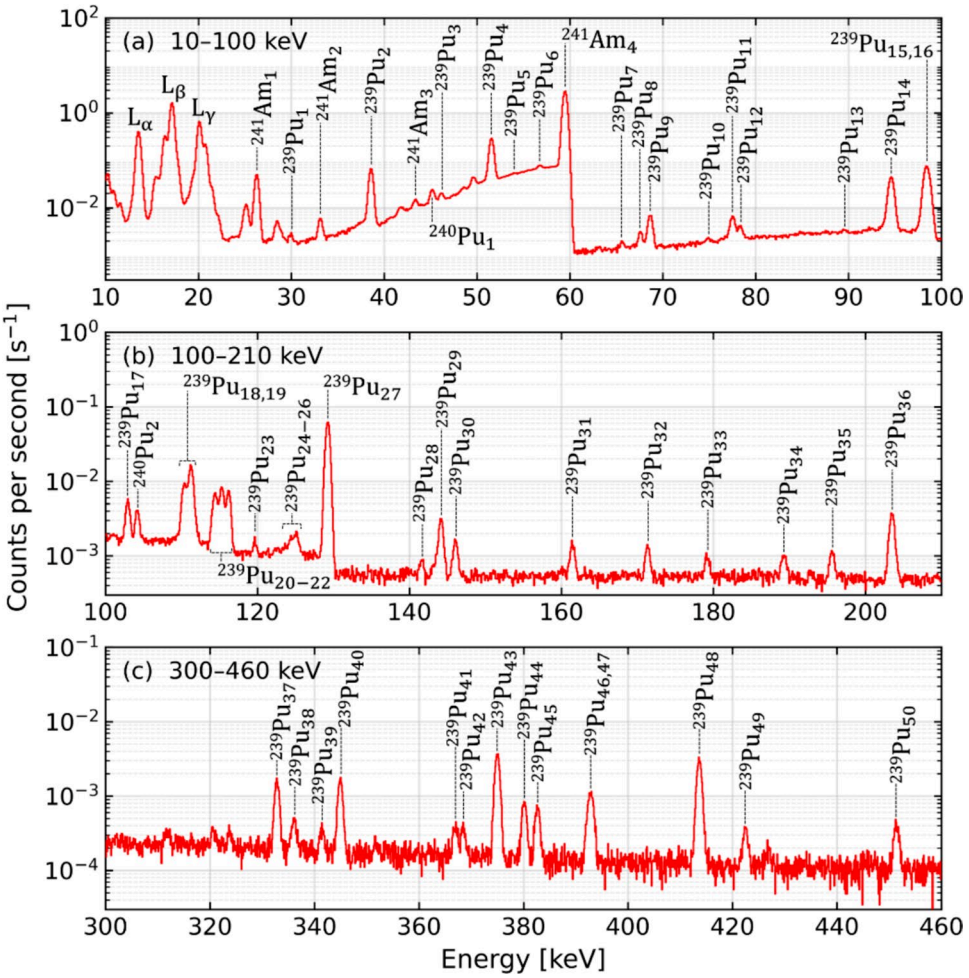

Fig. 10 Gamma-ray spectrum of the representative ^{239}Pu recoil-ion source 18. Identified transitions are labelled; corresponding energies and widths are provided in Table S2, Supplementary Information

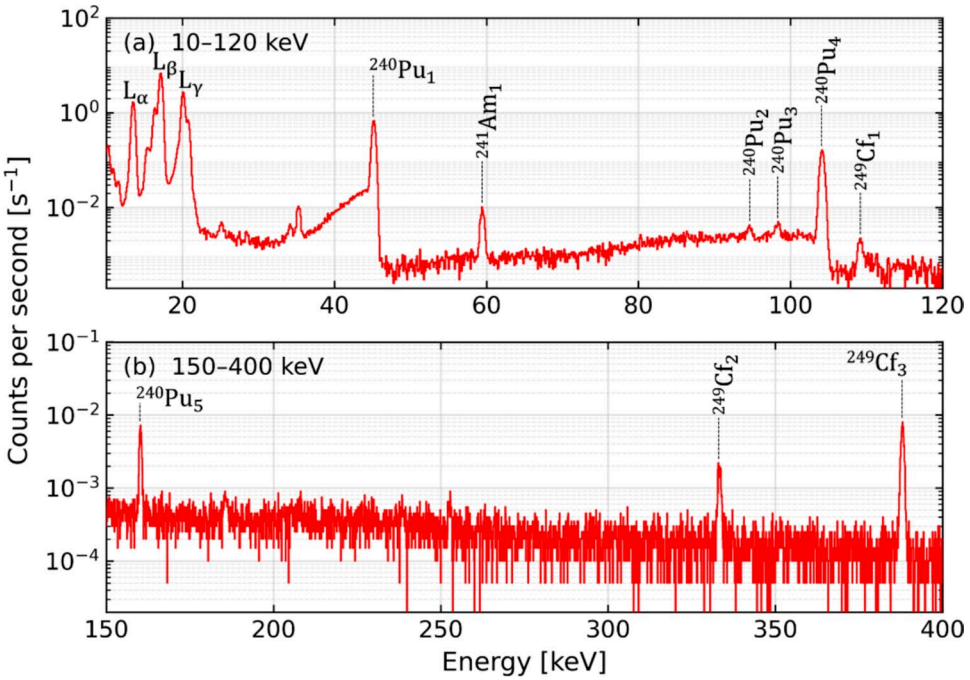

Fig. 11 Gamma-ray spectrum of the representative ^{240}Pu recoil-ion source 8c. Identified transitions are labelled; corresponding energies and widths are provided in Table S3, Supplementary Information

Tables S2 and S3 of the Supplementary Information. FWHM values consistently fell in the range 0.4–1.0 keV.

The ^{239}Pu source spectra exhibit dense line structures associated with decay to ^{235m}U, with the dominant lines at 52 keV, 34 keV and 129 keV. In contrast, ^{240}Pu sources exhibit a much simpler γ-spectrum, dominated by ^{236}U transitions at 45 keV, 104 keV and 160 keV [4, 13]. γ-transitions with emission probabilities below ~ 10^{-5}% were difficult to observe across all sources, indicating an effective detection limit. The majority of expected X-ray and γ-lines were assigned, with unassigned lines due to overlap with a dominant transition and the inability to deconvolve. No transitions associated with the decay of recoil daughters (e.g. ^{235}U at 186 keV and ^{236}U at 49 keV) were detected [18, 51]. ^{239}Pu spectra confirmed the presence of ^{241}Am, showing four characteristic γ-lines, with an ^{241}Am-to-^{239}Pu activity ratio of 1.2(1)% in excellent agreement with the α-derived and activity the decay-chain reconstructed activities. The two most intense lines of ^{240}Pu were detected, giving a ^{240}Pu-to-^{239}Pu activity ratio of 3.0(2)%, in agreement with the decay-corrected sample certification ^{240}Pu-to-^{239}Pu ratio of 3.3(1)%. ^{240}Pu spectra revealed the presence of α-decaying trace impurities below the limit of detection in α-spectrometry. ^{241}Am was observed via its characteristic 59.54 keV γ-line, with a ^{241}Am-to-^{240}Pu activity ratio of $1.6(7)\times10^{-3}$%, and trace ^{249}Cf was detected via its two most intense γ-lines at 333 keV and 388 keV and a $K\alpha_1$ X-ray emission at 109 keV, with a ^{249}Cf-to-^{240}Pu activity ratio of $1.8(1)\times10^{-3}$% [52]. The presence of ^{241}Am in sources is attributed to ^{241}Pu β-decay ingrowth, common in plutonium stock solutions. ^{249}Cf contaminant origin is unknown. It is not likely caused by any prior significant neutron irradiation of the material, since long-lived Cm isotopes would be observed (and ^{242}Pu, but its γ-lines overlap with ^{240}Pu γ-lines, hindering detection) [53].

Overall, the γ-ray spectrometry results were consistent among sources of the same isotope and supported the α-derived isotope composition. γ-ray energies show excellent agreement with evaluated nuclear data. The stability of the activity ratios across all sources and the close agreement

Table 4 ^{239}Pu, ^{240}Pu, ^{241}Am, and ^{249}Cf activities determined from γ-spectrometry for representative recoil-ion sources, derived from fitted γ-lines

Source ID	^{239}Pu Activity [kBq]	^{240}Pu Activity [kBq]	^{241}Am Activity [kBq]	^{249}Cf Activity [Bq]
1	48.7(4)	1.18(8)	0.490(10)	–
13	138.0(10)	3.0(3)	1.760(10)	–
16b	173.0(10)	5.6(5)	2.140(10)	–
18	197.0(10)	6.23(21)	2.230(10)	–
21	121.0(10)	3.85(23)	1.430(10)	–
4c	–	201.0(10)	0.00449(13)	3.51(15)
8c	–	393.0(20)	0.00356(12)	7.23(18)

between measured and decay-chain reconstructed activities indicate that isotopes are plated identically during MP [54]. Table 4 summarises source activity and composition determined by γ-spectrometry. Comparison of α- and γ-spectrometry activities shows strong consistency across all sources, with relative differences of 1–2% and all measurements agreeing within 1 σ.

Rutherford backscattering spectrometry results

RBS was performed at JYU on a subset of recoil-ion sources to determine elemental composition. Measurements were conducted using a 1.6 MeV He^{+} beam, with one source additionally analysed at 2.4 MeV He^{2+} to improve mass resolution and depth sensitivity for heavier elements. Spectra were acquired at a scattering angle of 160° by a ring of 14 Si PIPS detectors and evaluated using the JaBS simulation and fitting code [55]. Simulated spectra were fitted to experimental data by manually adjusting elemental concentrations, while layer thickness and roughness were fitted by the code. Due to normal incidence on Si substrates, channelling effects were present and accounted for; the substrate signal was not used in fluence normalisation and did not affect the reported results. Fluence was normalised using backscattering from a beam chopper and reference samples. The uncertainty in absolute Pu areal density is estimated to be less than 2%, including contributions from counting statistics, fitting, and systematic effects (e.g. beam energy and geometry). Uncertainties for other elements are significantly larger and more difficult to quantify.

All analysed sources exhibited thickness variation within the beam spot, with the largest deviations observed for thicker and more heterogeneous sources (e.g. source 21), consistent with RI results. For this source, the signal indicated that Pu was not at the surface, possibly due to residual solvent or post-deposition surface modification. Measurements at the source edges consistently showed higher Pu areal densities (≈ 10%) compared to central regions. This behaviour is consistent with the inhomogeneities observed by RI and supports the occurrence of edge accumulation effects during drying.

Elemental composition analysis was limited by mass resolution and the previously mentioned thickness variation. Contributions from ^{239}Pu and ^{241}Am could not be separated and are therefore treated as a combined signal. Similarly, other trace impurities identified by α- and γ-spectrometry (e.g. ^{249}Cf) are below the detection sensitivity of RBS. Additional trace elements were detected, including S, Ca, Fe (including unresolved Ni/Cr contributions), and Zn. The ^{240}Pu source 8c exhibited an additional weak signal tentatively assigned to La based on best-fit criteria; however, this assignment remains uncertain due to mass overlap. No La could be detected by γ-spectrometry of the same source. All samples contained C and O. Quantification of O was complicated by overlap with the substrate signal, but an approximate O-to-Pu ratio of 6–7 was obtained. The C quantification is less reliable due to RBS's limited sensitivity to C; however, the fit suggests a C-to-Pu ratio of ~ 4. Figure 12 shows experimental and simulated RBS histograms for a ^{240}Pu recoil-ion source, demonstrating good agreement between the measurement and the fit.

^{228}Th-spiked ^{239}Pu recoil-ion source preparation and characterisation

Imaging results

Seven ^{228}Th-spiked ^{239}Pu recoil-ion sources were prepared on Si substrates by MP (Fig. 13), with thicknesses ranging

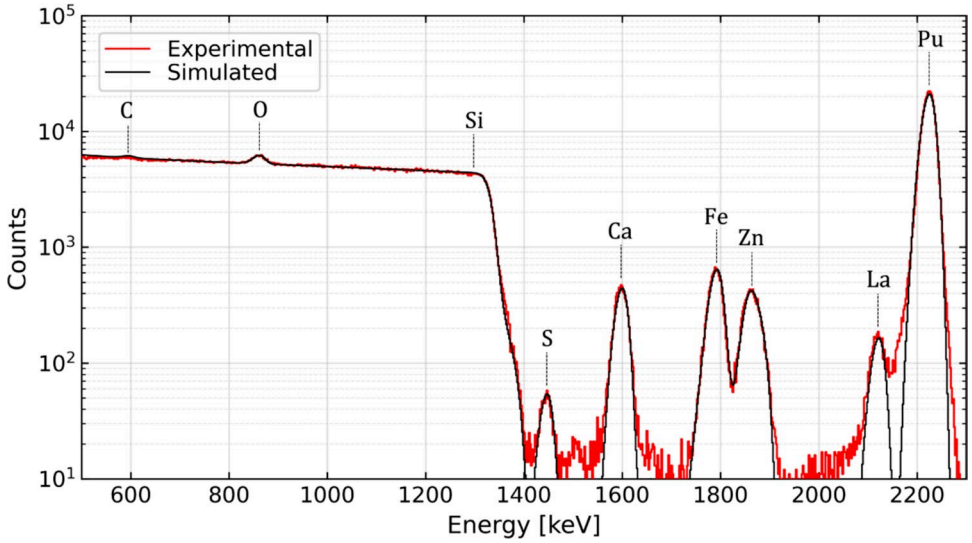

Fig. 12 Experimental (red) and simulated (black) RBS histograms of ^{240}Pu recoil-ion source 8c on Si substrate. Experimental data was measured with a 2.4 MeV He^{2+} beam

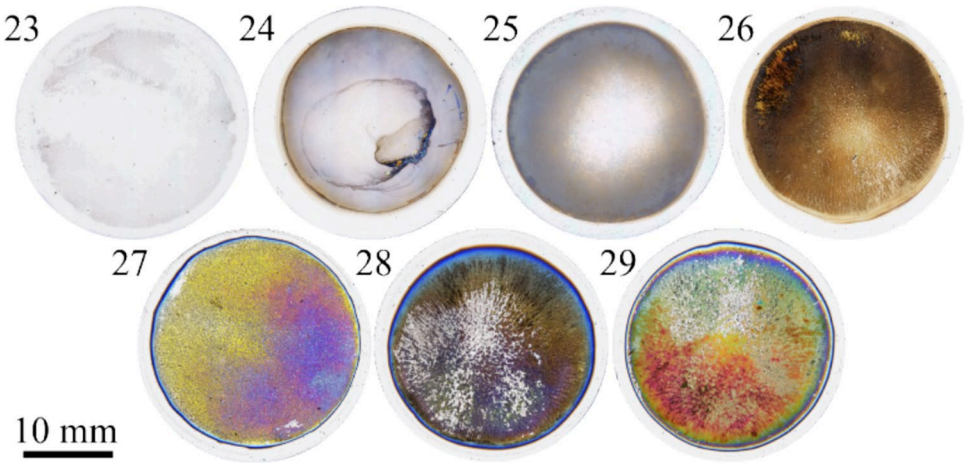

Fig. 13 Optical photographs of ^{228}Th-spiked.^{239}Pu recoil-ion sources on Si substrates produced by molecular plating, labelled by source ID as given in Table 1

Table 5 Thickness, active area, ^{239}Pu, ^{241}Am and ^{228}Th activity, and activity density histogram centroid and full width at half maximum (FWHM) values for ^{228}Th-spiked ^{239}Pu recoil-ion sources produced by molecular plating. Source ID as given in Table 1

Source ID	Thickness [nm]	Area [mm^2]	^{239}Pu Activity [kBq]	^{241}Am Activity [kBq]	^{228}Th Activity [kBq]	Centroid Activity [Bq mm^{-2}]	FWHM [Bq mm^{-2}]
23	6.4(9)	8.2(3)	0.34(5)	0.0037(5)	1.10(12)	920(50)	99(8)
24	15.2(12)	269(11)	27.7(23)	0.297(24)	1.27(14)	211(13)	130.0(10)
25	24.7(23)	261(10)	45(4)	0.48(5)	0.83(9)	314(23)	205(3)
26	45(4)	267(11)	82(7)	0.87(8)	1.05(16)	560(40)	264(4)
27	100(10)	294(12)	192(20)	2.05(22)	1.45(12)	1210(100)	331(7)
28	115(9)	242(10)	196(15)	2.10(16)	1.5(8)	1410(90)	1350(9)
29	149(13)	256(10)	266(24)	2.9(3)	2.0(4)	1800(500)	1506(7)

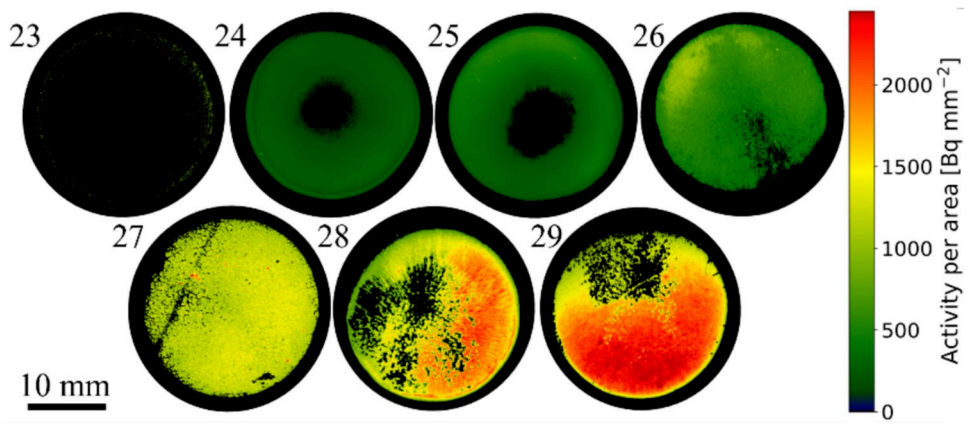

Fig. 14 Radiographic activity density maps of ^{228}Th-spiked ^{239}Pu recoil-ion sources, labelled by source ID as given in Table 1

from 6 to 149 nm (Table 5). The observed colour variations across the sources were found to correlate with thickness and activity distributions and are consistent with thin-film interference effects. Compared to the unspiked ^{239}Pu sources (Imaging results,^{239}Pu and^{240}Pu recoil-ion source preparation and characterisation section), the spiked sources extend to lower thicknesses, where a transition from blue to yellow/gold is observed. At higher thicknesses, a transition from green to red is observed, and colour variation within individual sources increases, reflecting the growing spatial inhomogeneity in RI activity density maps (Fig. 14).

RI activity density and 3D thickness maps (Fig. S6, Supplementary Information) demonstrate a clear evolution in layer morphology with increasing thickness. For the thinnest sources, activity distributions remain relatively uniform across the active area, and the corresponding

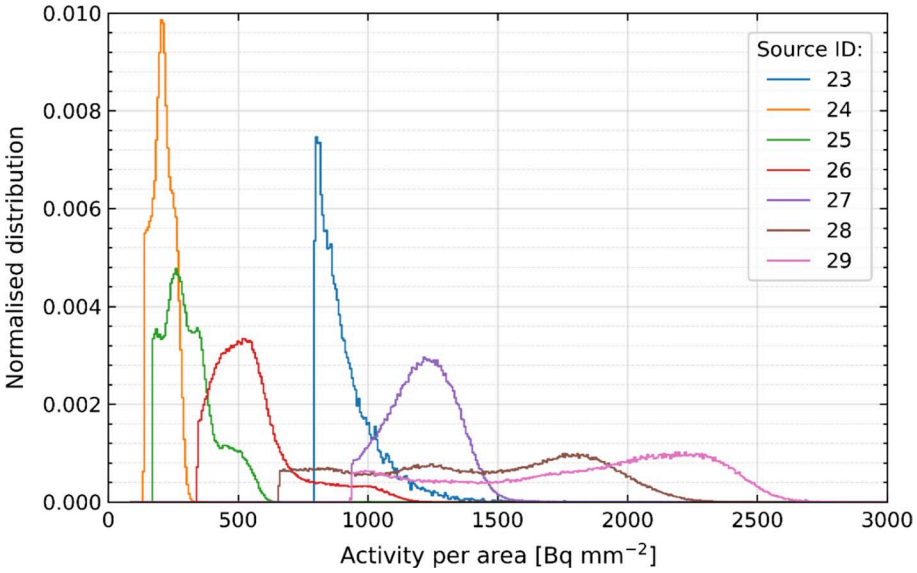

Fig. 15 Activity density histograms derived from radiographic imaging of ^{228}Th-spiked ^{239}Pu recoil-ion sources, with legend source ID as given in Table 1. Histograms were normalised such that the total area under each distribution equals unity. Homogeneous sources have sharper, more symmetric, and well-defined peaks

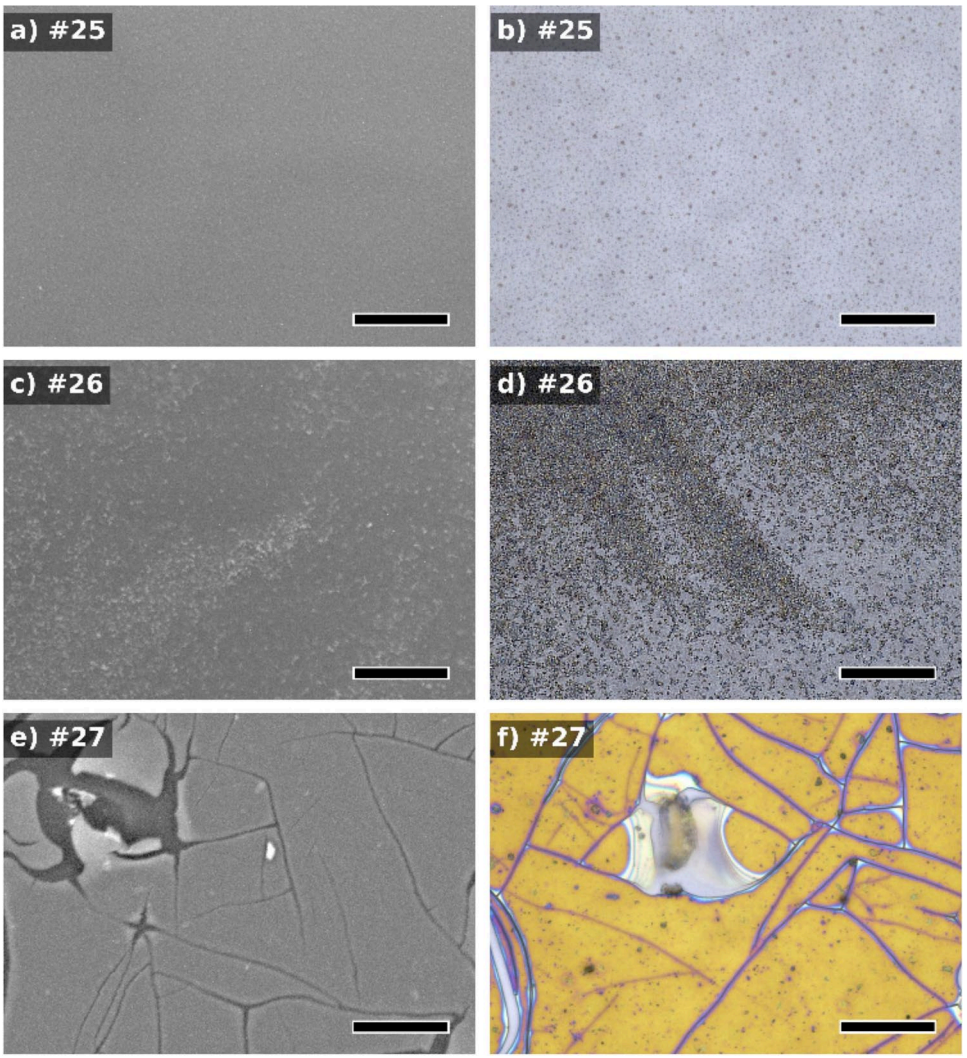

Fig. 16 Scanning electron microscopy (SEM) secondary electron (left) and laser scanning microscopy (LSM) (right) images of representative ^{228}Th-spiked ^{239}Pu recoil-ion sources, labelled by their source ID as given in Table 1, from thinnest (top row) to thickest (bottom row). (**f**) is SEM backscattered electron (BSE). Scale bar: 20 µm

histograms are narrow and symmetric, consistent with homogeneous films. Histograms are shown in Fig. 15, with areal activity centroids and FWHM values summarised in Table 5. As thickness increases, spatial inhomogeneity becomes more apparent, the activity maps reveal visible gradients and localised regions of elevated activity, and the histograms broaden and develop increasing asymmetry, indicating greater variance in local thickness. Quantitative metrics, including coverage, dispersion, skewness, and kurtosis, support this trend. Source 23 shows limited areal coverage and a strongly right-skewed distribution with high kurtosis, consistent with incomplete film formation. In contrast, sources 24–26 exhibit improved coverage and more continuous films, although dispersion values suggest the onset of localised thickening in sources 25 and 26. Source 27 has the highest coverage and lowest dispersion and is therefore the most uniform film in the series. At greater thicknesses (sources 28–29), spatial variability increases, with broader, flatter distributions indicating the development of macroscopic thickness gradients. Based on combined coverage and distribution metrics, the sources, in order of decreasing homogeneity, were 27, 24, 25, 26, 29, and 28, with source 23 excluded due to incomplete coverage.

Surface morphology was investigated using SEM and LSM. Both techniques are in good qualitative agreement, with LSM providing additional contrast for surface features not readily resolved by SEM imaging (Fig. 16). A clear thickness-dependent evolution in morphology is observed, consistent with and extending the trends identified for the unspiked ^{239}Pu and ^{240}Pu sources (Imaging results, ^{239}Pu and ^{240}Pu recoil-ion source preparation and characterisation section).

LSM shows that for thinner layers ($\leq$ 45 nm; sources 23–26), films initially form via island-like growth with localised clustering, resulting in regions of varying density (Figs. 16b and 17a). With increasing thickness, these features coalesce into microscale sheet-like structures and evolve into largely continuous films (Fig. 17b–f). This behaviour is consistent with the early-stage coalescence of a thin-layer formation following initial nucleation [40]. At larger thicknesses ($\geq$ 100 nm; sources 27–29), pronounced surface inhomogeneities developed. LSM showed the formation of extended cracking, spatially correlated with thicker regions of the layer, consistent with observations from literature and with the increased heterogeneity observed in RI analysis [56, 57]. In thinner regions of these sources, isolated or sinuous cracks are observed, whereas in thicker regions they evolve into interconnected crack networks (Fig. 17g–j). Two characteristic crack types are identified: large openings exposing the substrate and finer hairline cracks, which often connect larger fracture regions. In heavily affected areas, delamination and localised peeling of the layer occurred. (Fig. 17j).

Crack initiation was frequently associated with circular void-like regions from which fracture networks appear to propagate. Within these void-like regions, a darker, diffuse structure was usually observed. The structures appear to be located at or near the substrate interface and often appear to have ruptured through the layer. Similar structures are observed along crack boundary paths. In some cases, fine-scale features appear to be locally concentrated around these sites, consistent with clustering behaviour observed during earlier stages of film formation. The origin of the observed cracking and void-associated features cannot be uniquely determined from the present data; however, several mechanisms may contribute. These include that another layer was starting to grow underneath the continuous layer, perhaps due to some trapped MP solvent, which would take longer to dry at deeper depths, causing larger cluster growth; well-known stress-induced cracking and delamination caused by solvent evaporation or phase separation during drying after MP; and H_2 accumulation at defect or interface sites, causing rupture [56–59]. For the latter, H has been found to accumulate preferentially at the Si-to-metal layer interface, with H atoms able to diffuse through the layer [44]. The increased extent of cracking relative to unspiked ^{239}Pu and ^{240}Pu sources may indicate that the incorporation of ^{228}Th or its decay products influences film stability; however, this cannot be conclusively established here. Additional examples are provided in Fig. S7 of the Supplementary Information.

Alpha-spectrometry results

Alpha-particle spectrometry showed that the ^{228}Th-spiked ^{239}Pu recoil-ion sources contained 0.8–2.0 kBq of ^{228}Th and 0.34–266 kBq of ^{239}Pu, corresponding to reconstructed layer thicknesses of 6 to 149 nm. The measured ^{241}Am-to-^{239}Pu activity ratio was 1.07(4)%, consistent across all sources. The average indirect MP yield, determined from depletion of activity in the plating solution for the ^{228}Th-spiked ^{239}Pu and ^{228}Th sources was 88(1)%, comprising 86(1)% for ^{239}Pu and 89(1)% for ^{228}Th. In contrast, the corresponding direct yields, determined from measured source activities, were significantly lower, averaging 63(3)% and comprising of 61(3)% for ^{239}Pu and 65(5)% for ^{228}Th. This corresponds to an overall reduction of 27(3)% between indirect and direct yields, with reductions of 25(3)% and 28(5)% for ^{239}Pu and ^{228}Th, respectively. The close agreement between ^{239}Pu and ^{228}Th within indirect and direct yield determinations indicates proportional co-deposition during MP. However, unlike the unspiked ^{239}Pu and ^{240}Pu sources (Alpha-spectrometry results, ^{239}Pu and ^{240}Pu recoil-ion source preparation and characterisation section), where direct and indirect

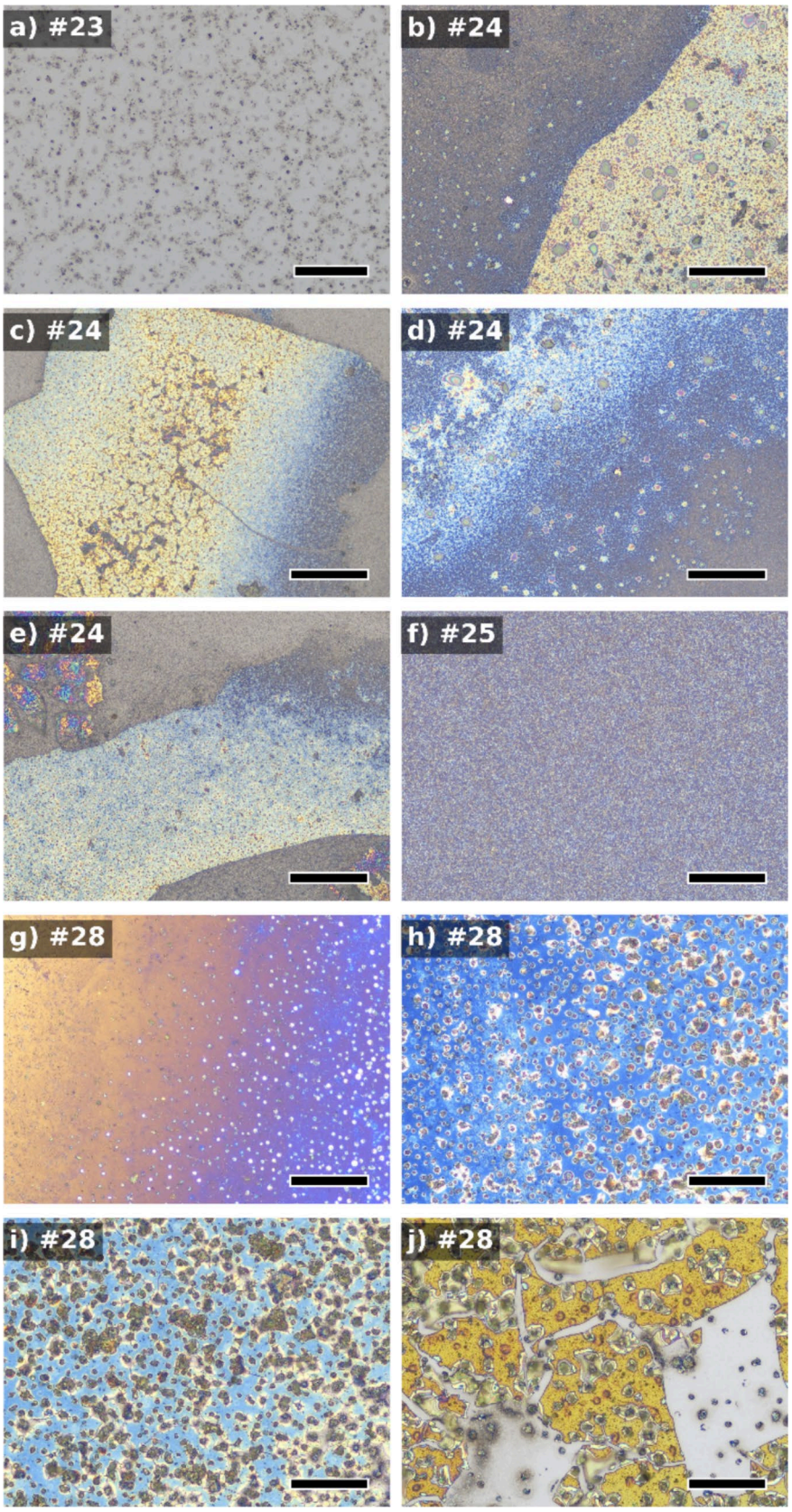

Fig. 17 Laser scanning microscopy (LSM) images in optical mode (coaxial illumination) of representative ^{228}Th-spiked ^{239}Pu recoil-ion sources taken ~ 3 months after preparation, labelled by source ID as given in Table 1. Panels show selected source regions showing thickness-dependent morphology and defect structures: (**a**–**e**) layer formation; (**f**) centre; (**g**–**j**) edge-to-centre. Scale bar: 40 µm. Additional images provided in Fig. S7, Supplementary Information

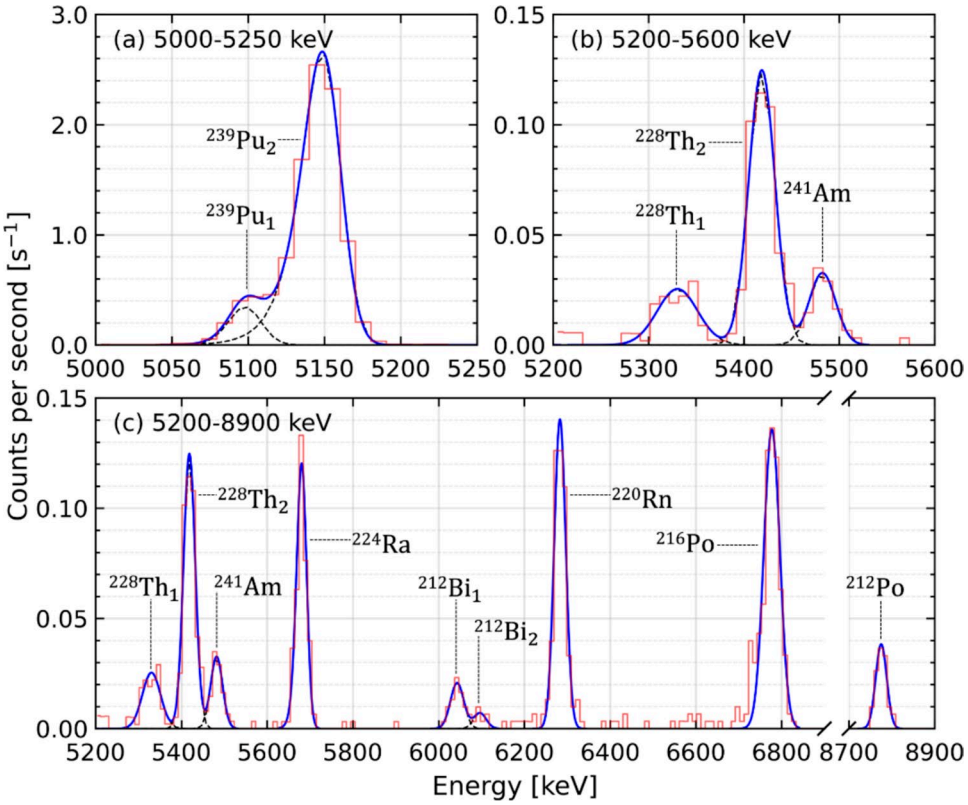

Fig. 18 Alpha-particle spectrum of the representative ^{228}Th-spiked ^{239}Pu recoil-ion source 24. Measured spectra (red solid histogram), total peak fits (bold blue solid), and individual peak components (black dashed) are shown. Panels (**a**) and (**b**) show the ^{239}Pu doublet and ^{228}Th/^{241}Am triplet, with decomposition. Panel (**c**) shows ^{241}Am and the ^{228}Th-spike with its decay chain daughters, much less intense than the ^{239}Pu signal. ^{239}Pu, ^{241}Am, ^{228}Th and its subsequent decay-chain daughter peaks are identified and labelled

yields agreed, the spiked sources show a systematic reduction in ^{239}Pu and ^{228}Th direct yields relative to indirect yields. Similar behaviour has been observed at the JGU for independently plated Th sources across a range of isotope compositions and plating parameters. In contrast, U, Am, and Pu typically exhibit high and well-matched yields, even when co-deposited. This suggests that Th exhibits distinct MP behaviour compared to neighbouring actinides and may influence both deposition and retention of co-plated nuclides. Possible explanations include Th-influenced enhanced adsorption of isotopes on cell surfaces, leading to overestimation of indirect yields, and/or Th-influenced reduced layer stability on the substrate, resulting in partial loss of material during post-plating handling after the post-plating aliquot is taken for indirect yield measurements (i.e. during removal of the plating solution from the cell during disassembly). For all subsequent activity calculations, the activity inferred from direct measurements was used.

The representative α-particle spectrum shown in Fig. 18 shows clear identification of ^{239}Pu, ^{228}Th, ^{241}Am, ^{224}Ra,

Table 6 Experimentally inferred (exp. inf.) and predicted (pred.) ^{224}Ra recoil escape efficiencies (eff.), as well as corresponding ^{224}Ra area-normalised recoil rates for the ^{228}Th-spiked ^{239}Pu recoil-ion sources. Recoil rates are derived from corresponding escape efficiencies, the source area (from radiographic imaging analysis), and the measured ^{228}Th mother-spike activity, which is nearly constant. Predictions were obtained from the model used to fit Geant4-simulated escape efficiency data as a function of source thickness. Full details of the simulation, fitting models and experimental measurements for escape efficiencies are given in [25]

Source ID	Thickness [nm]	^{228}Th Activity [kBq]	Exp. Inf. ^{224}Ra Escape Eff. [%]	Pred. ^{224}Ra Escape Eff. [%]	Exp. Inf. ^{224}Ra Recoil Rate [s^{-1} cm^{-2}]	Pred. ^{224}Ra Recoil Rate [s^{-1} cm^{-2}]
23	6.4(9)	1.10(12)	61(8)	65(8)	8000(1000)	9000(1000)
24	15.2(12)	1.27(14)	33(4)	48(4)	155(25)	230(32)
25	24.7(23)	0.83(9)	40(9)	34(9)	130(32)	110(31)
26	45(4)	1.05(16)	18.2(20)	19.6(20)	72(14)	77(15)
27	100(10)	1.45(12)	8.0(10)	9.0(10)	40(9)	42(9)
28	115(9)	1.5(8)	7(4)	7(4)	40(31)	40(32)
29	149(13)	2.0(4)	8.0(10)	5.0(20)	58(15)	41(14)

Table 7 Experimentally validated ^{235m}U recoil escape efficiency (eff.) predictions and corresponding area-normalised ^{235m}U recoil rate for the ^{239}Pu and ^{228}Th-spiked ^{239}Pu recoil-ion sources. The dashed black line after source ID 22 denotes the start of the ^{228}Th-spiked ^{239}Pu recoil-ion source set. Recoil rates are derived using escape efficiency, source area (from radiographic imaging analysis) and measured ^{239}Pu mother activity. Predictions were obtained from the validated model used to fit Geant4-simulated escape efficiency data as a function of source thickness, full details of which are given in [25]. Statistical, $\sigma_{stat,}$ and systematic, $\sigma_{syst,}$ uncertainty contributions to the ^{235m}U recoil-rate total uncertainty are also reported

Source ID	Thickness [nm]	^{239}Pu Activity [kBq]	^{235m}U Escape Eff. [%]	^{235m}U Recoil Rate [s^{-1} cm^{-2}]	σ_{stat} [s^{-1} cm^{-2}]	σ_{syst} [s^{-1} cm^{-2}]
1	24.0(16)	48(3)	32.6(22)	4500(400)	208	422
2a	25.3(17)	52(4)	31.1(20)[1]	4600(400)	210	417
3	29.8(20)	55(4)	27.0(17)	4700(400)	207	420
5b	35.8(24)	70(5)	22.8(15)	4700(500)	203	448
7	50(3)	99(7)	16.4(12)	4800(500)	202	476
9b	51(3)	101(7)	16.1(12)	4800(500)	199	484
10	61(4)	70(5)	13.4(10)	4700(500)	189	479
11	64(4)	69(5)	12.7(10)	4700(500)	211	481
12	64(4)	134(9)	12.7(11)	4700(500)	199	502
13	65(4)	137(9)	12.4(10)	4700(500)	196	500
14a,b	68(5)	142(10)	11.9(10)[1]	4700(500)	198	500
15	78(5)	153(10)	10.3(9)	4600(500)	198	512
16b	83(6)	172(12)	9.6(9)	4600(500)	197	514
17a	89(7)	185(14)	8.9(9)[1]	4600(600)	200	568
18	97(7)	197(14)	8.0(8)	4500(500)	198	529
19	100(7)	206(14)	7.8(8)	4500(500)	194	526
20	105(7)	123(9)	7.3(7)	4500(600)	191	543
21	107(5)	121(6)	7.2(6)	4400(500)	210	440
22	108(7)	119(8)	7.1(7)	4400(600)	204	535
23	6.4(9)	0.34(5)	65(5)	2700(400)	408	147
24	15.2(12)	27.7(23)	47(3)	4800(500)	446	343
25	24.7(23)	45(4)	32(3)	5400(700)	500	526
26	45(4)	82(7)	18.4(16)	5600(700)	487	567
27	100(10)	192(20)	7.8(10)	5100(900)	554	703
28	115(9)	196(15)	6.6(7)	5400(700)	404	650
29	149(13)	266(24)	4.9(7)	5100(900)	447	772

[1]Sources deposited on Ti substrate; Si-based simulations used (negligible substrate effect at these thicknesses)

and subsequent decay chain daughters. As layer thickness increases, the spectra show progressive peak broadening and reduced peak separation, particularly within the ^{228}Th–^{241}Am multiplet region (see Fig. 2 in Source characterisation, Experimental section). This behaviour reflects increased self-absorption and energy straggling in thicker layers. Peak fitting, however, remained stable across all sources, with $R^2 \geq 0.95$. The fitted peak energies and FWHM values (Table S4, Supplementary Information) agree with reference data within the stated uncertainties. Overall, α-particle spectrometry confirms the expected isotopic composition and that MP was performed well. Consistent

differences between direct and indirect yields were observed and are attributed to the addition of ^{228}Th, which may influence source formation and warrants further investigation.

^{224}Ra and ^{235m}U recoil escape efficiency

For the experimentally inferred ^{224}Ra recoil escape efficiency, five of the seven measurements fall within ± 1 σ of the model prediction, and six fall within ± 1.5 σ. Both experimentally inferred and model-predicted ^{224}Ra recoil escape efficiency values are summarised in Table 6 and plotted with the model fit in Fig. S8 of the Supplementary Information. A single outlier occurring at T ≈ 15 nm (source 24) has a standardised residual of -4.3 σ and dominates the total squared deviation. With the outlier excluded, the RMS deviation is 3.28(95)%, the reduced χ^2 is 0.54, and the mean residual is 0.46%, supporting good agreement between the model and experiment. Importantly, the majority of unspiked ^{239}Pu sources fall within the T ≳ 25 nm regime, where the model reproduces values at the 1.29(46)% level, supporting its use to determine ^{235m}U recoil escape efficiencies. Simulations also found that substrate composition has a negligible influence on recoil escape efficiency in this thickness range [25], justifying the use of simulations performed for Si substrates when evaluating Ti-backed sources. The model predicted a mean stopping distance of 14.0(2) nm for ^{224}Ra recoils in a ^{239}Pu layer.

Using the experimentally inferred ^{224}Ra recoil escape efficiency and model-predicted escape efficiency, the corresponding ^{224}Ra recoil rates for each source thickness were calculated, summarised in Table 6, and plotted in Fig. S9 of the Supplementary Information. The mean normalised deviation was 0.55 σ, with a maximum deviation of 1.87 σ between experimentally inferred and model-predicted recoil rates. In general, the ^{224}Ra recoil rate decreases with increasing source thickness. This behaviour arises because the ^{228}Th mother is introduced as a spike and remains nearly constant across all sources, while the ^{239}Pu layer thickness varies. Consequently, as the layer thickness increases, the same ^{228}Th activity is distributed over a larger volume. Following each ^{228}Th decay, an increasing fraction of ^{224}Ra recoils are therefore born at depths exceeding their escape range, reducing the recoil rate. A sharp drop in recoil rate, followed by a transition to a "tailing" regime dominated by geometric dilution, is observed in the thickness range of ~ 30–60 nm. Across all Geant4 simulations, the average maximum birth depth for recoils that escape was determined to be 40.0(6) nm, in good agreement with the experimentally observed transition to the tailing regime in the ~ 30–60 nm thickness range.

Using the validated escape efficiency model with the simulated ^{235m}U recoil escape efficiency, experimental predictions of ^{235m}U recoil escape efficiency for both the ^{228}Th-spiked ^{239}Pu source and the unspiked ^{239}Pu source thicknesses, summarised in Table 7 and plotted with the model fit in Fig. S10 of the Supplementary Information, could be determined. The ^{236}U recoil escape efficiency experimental predictions for the ^{240}Pu sources, given in Table 8, were based on ^{235m}U recoil escape simulations, used for computational efficiency, as the ^{236}U recoil energy differs by only ~ 0.3 keV from the ^{235m}U recoil energy. Given this, ^{236}U recoil transport in ^{240}Pu layers is expected to closely approximate ^{235m}U recoil behaviour in ^{239}Pu layers of equivalent thickness. The simulated and fitted ^{235m}U escape efficiency as a function of ^{239}Pu layer thickness showed the same thickness-dependent behaviour as the simulated and fitted ^{224}Ra escape efficiency as a function of ^{239}Pu layer thickness. The model predicts a mean stopping distance of 13.2(3) nm for ^{235m}U recoils in ^{239}Pu layers. For thicknesses T ≳ 25 nm, escape efficiencies enter a "tailing" regime dominated by geometric dilution, where an increasing fraction of recoils is generated at depths beyond their escape range. A detailed account of the simulation and fitting models for escape efficiency, including an explanation of trends and substrate-dependent behaviour, is given in [25].

The area-normalised ^{235m}U recoil rates obtained using the ^{235m}U recoil escape efficiency predictions are given in Table 7 and plotted in Fig. 19a and c for the unspiked ^{239}Pu and the ^{228}Th-spiked ^{239}Pu recoil-ion sources, respectively. The area-normalised ^{236}U recoil rates are summarised

Table 8 Experimentally validated ^{236}U recoil escape efficiency (eff.) predictions for ^{240}Pu recoil-ion sources. Corresponding area-normalised recoil rate is calculated using the source area (from radiographic imaging analysis) and the measured ^{240}Pu mother activity. Full details of the simulation used to obtain escape efficiency results are given in [25]. Statistical, $\sigma_{stat,}$ and systematic, $\sigma_{syst,}$ uncertainty contributions to the ^{236}U recoil-rate total uncertainty are also reported

Source ID	Thickness [nm]	^{240}Pu Activity [kBq]	^{236}U Escape Eff. [%]	^{236}U Recoil Rate [s^{-1} cm^{-2}]	σ_{stat} [s^{-1} cm^{-2}]	σ_{syst} [s^{-1} cm^{-2}]
4c	28.2(16)	213(13)	28.3(16)[2]	17,000 (1000)	744	1360
6a,c	48(3)	367(21)	17.2(11)[1,2]	18,000(2000)	735	1563
8c	50(3)	392(23)	16.3(11)[2]	18,000(2000)	752	1590

[1]Sources deposited on Ti substrate; Si-based simulations used (negligible substrate effect at these thicknesses)

[2]Escape efficiencies used from ^{239}Pu simulations for ^{235m}U recoils due to similar recoil energy (~ 0.3 keV difference)

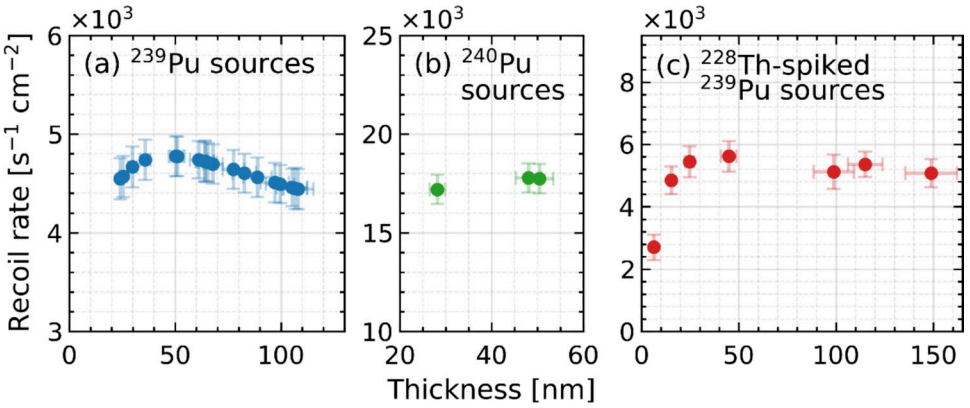

Fig. 19 Area-normalised ^{235m}U (**a**, **c**) and ^{236}U (**b**) recoil rates as a function of source thickness for (**a**) ^{239}Pu, (**b**) ^{240}Pu and (**c**) ^{228}Th-spiked ^{239}Pu recoil-ion sources. Rates are derived using experimentally validated escape efficiencies, source areas (from radiographic imaging analysis) and measured Pu mother activities. ^{236}U recoil rates in (**b**) are much higher than (**a**) and (**c**) due to the shorter half-life of the mother, ^{240}Pu

in Table 8 and plotted in Fig. 19b for the ^{240}Pu recoil-ion sources. Raw ^{235m}U recoil rate data for ^{239}Pu and ^{228}Th-spiked ^{239}Pu recoil-ion sources, as well as raw ^{224}Ra recoil rate data for ^{228}Th-spiked ^{239}Pu recoil-ion sources, are given in Table S5 of the Supplementary Information. Raw ^{236}U recoil rate data for ^{240}Pu recoil-ion sources are given in Table S6 of the Supplementary Information. Both statistical and systematic uncertainty contributions to the ^{235m}U and ^{236}U recoil rate are reported for all sources. The systematic uncertainty for the unspiked ^{239}Pu and ^{240}Pu sources was dominated by the ^{241}Am activity calibration uncertainty (30%), determined from the calibration certificate, leading to an overestimation of the total uncertainty. As such, all recoil rate plots in Fig. 19 are plotted using their statistical uncertainty. The ^{235m}U recoil rate exhibits a different thickness dependence than the ^{224}Ra recoil rate trend, since the recoil mother activity is not a spike but increases with source thickness. For ^{239}Pu recoil-ion sources, the raw recoil rate (s^{-1}) is lower for 16 mm diameter sources compared to 22 mm sources of similar thicknesses, reflecting their smaller active area and correspondingly lower ^{239}Pu activity. When both unspiked ^{239}Pu and the ^{228}Th-spiked ^{239}Pu recoil-ion source ^{235m}U recoil rates are normalised for source area, a clear thickness-dependent trend emerges. From thin thicknesses, the recoil rate increases with increasing layer thickness. This reflects the increasing ^{239}Pu areal activity, and thus the number of ^{235m}U recoils, of which a large fraction is still born within the escape depth and can leave the layer. At intermediate thicknesses (~40–55 nm), the recoil rate reaches a maximum. This corresponds to the maximum recoil escape depth, where all recoils are born at a depth from which escape remains possible. For larger thicknesses, the recoil rate decreases despite the continued increase in ^{239}Pu activity. Here, an increasing fraction of recoils is produced at depths exceeding the escape range, leading to geometric dilution of the escaping fraction, similar to the "tailing" region observed for escape efficiency. Across all simulations, ^{235m}U recoils that escaped had a maximum birth depth of 63.6 nm, with an average maximum depth of 44.2(42) nm, consistent with the observed peak in recoil rate at ~40–55 nm source thickness. The ^{236}U recoil rates appear to peak in the same thickness range and are much higher at comparable thicknesses due to the shorter mother half-life and higher mother activity used. A small systematic offset can be observed between the unspiked ^{239}Pu and the ^{228}Th-spiked ^{239}Pu recoil-ion source ^{235m}U recoil-rate datasets, and this is attributed to different α-activity measurement systems and calibration standards used for each source type measurement. For the optimisation of recoil-ion sources, the highest possible recoil rate must be achieved so that the number of recoils escaping is sufficient for, e.g., CLS studies. Based on the present work, we can say that ^{239}Pu and ^{240}Pu recoil-ion sources with ~40–55 nm layer thicknesses yield the highest ^{235m}U and ^{236}U recoil ion rates per unit area, respectively. Peak ^{236}U recoil ion rates per unit area occurred at a layer thickness similar to that of peak ^{235m}U rates and were ~3.7 t larger due to the mother's shorter half-life and higher activity at similar thicknesses.

Conclusions

This work systematically investigated the preparation and characterisation of ^{239}Pu, ^{240}Pu and ^{228}Th-spiked ^{239}Pu recoil-ion sources produced via MP, with the primary objectives of investigating, quantifying, and optimising the recoil escape efficiency from recoil-ion sources - particularly for ^{235m}U recoil ions to enable the study of this isomer.

The results demonstrate that MP using DMF is a highly reliable and reproducible method for producing actinide thin films, achieving consistently high deposition yields (~94–97%) and identical plating across different isotopes. Comprehensive multi-technique characterisation (RI, SEM, LSM, α- and γ-spectrometry, and RBS) provided insight into thin-film formation and morphology that affect layer quality and thus govern recoil source performance.

A clear thickness-dependent evolution was identified across all datasets. Thin layers (~24–84 nm) exhibited the

highest homogeneity, smoothest morphology, and minimal defect density. In contrast, thicker films (> 90 nm) showed increased inhomogeneity, edge activity, and thickness accumulation ("coffee-ring" effects), cracking, and visible defect formation. These structural changes likely arise from a combination of deposition dynamics, solvent drying processes, and possible gas-induced effects (e.g. H_2-related blistering). Substrate material and drying conditions had comparatively minor influence on large-scale activity distributions but could affect local morphology: layers on Ti showed less cracking and fewer defects than comparable films on Si substrates, and oven-drying appeared to increase the size and frequency of defects in occasional localised areas. A wide variety of colours were observed and shown to correlate with thickness, indicating that colour and colour variation in thin films can provide insights into their homogeneity by eye alone.

RI combined with decay-chain-informed thickness reconstruction proved to be a powerful and non-destructive method for resolving thickness distributions, enabling quantitative assessment of homogeneity and its evolution with thickness. RBS and LMS agreed with these homogeneity findings.

A key outcome of this work is the validated methodology for determining recoil escape efficiencies. By using ^{224}Ra recoil collection efficiency data from the ^{228}Th-spiked ^{239}Pu sources as a surrogate system, we could produce experimentally inferred ^{224}Ra recoil collection efficiencies, and when compared to simulations, were shown to reproduce experimentally inferred ^{224}Ra escape efficiencies at the ~ 3% level. This validation enabled reliable determination of ^{235m}U recoil escape efficiencies across the full thickness range of ^{239}Pu sources.

The recoil escape behaviour follows a well-defined thickness dependence a rapid decline with increasing thickness is observed as bulk stopping within the layer dominates. For thicknesses $T \gtrsim 25$ nm, escape enters a geometric "tailing" regime, where an increasing fraction of recoils are born beyond their escape range.

This behaviour directly governs the recoil ion emission rates. For the ^{228}Th-spiked ^{239}Pu sources, where the ^{228}Th mother activity is approximately constant, the ^{224}Ra recoil rate drops sharply with increasing thickness, before transitioning to a "tailing" regime due to geometric dilution. In contrast, for ^{239}Pu and ^{240}Pu sources, the increasing mother activity with thickness leads to a competing effect: the recoil rate per unit area initially rises, reaches a maximum when the layer thickness becomes comparable to the maximum recoil escape depth, and subsequently decreases as escape losses dominate. As a result, an optimal ^{239}Pu and ^{240}Pu thickness range of ~ 40–55 nm is identified, corresponding to the maximum recoil rate per unit area for both ^{235m}U and ^{236}U. At this thickness, the balance between increasing mother activity and decreasing escape probability is optimised. The higher recoil rates observed for ^{236}U (by a factor of ~ 3.7) are attributed to the shorter half-life and correspondingly higher activity of the ^{240}Pu mother.

The ~ 40–55 nm thickness at which the optimum recoil rate per unit area occurs for both ^{239}Pu and ^{240}Pu recoil-ion sources fits nicely inside the ~ 24–84 nm range where layers were observed to be the most homogeneous. Sources with larger deposition areas were found not only to increase the total recoil rate but also to be consistently more homogeneous than sources of smaller deposition areas at comparable thicknesses. The effect of substrate on recoil rate is negligible in the ~ 40–55 nm range; however, overall, fewer defects were observed for sources on Ti compared to Si substrates of comparable thicknesses. This may result from hydrogen evolution on Si substrates and/or increased Ti roughness, which may improve layer adherence.

Therefore, this work has shown that the optimum ^{239}Pu and ^{240}Pu recoil-ion sources produced by MP with DMF in this study have thicknesses of ~ 40–55 nm, are on Ti substrates, have larger deposition areas and are air-dried after plating. This combination of parameters yields the highest recoil rates of ^{235m}U and ^{236}U per unit area, as well as the best layer homogeneity and morphology across the full thickness range.

The work also highlights limitations in co-deposition systems involving Th, where significantly reduced direct yields of both isotopes in the system, Th and Pu, indicate altered plating behaviour, and sources to show extensive cracking and delamination, uncharacteristic of comparable unspiked ^{239}Pu layers, suggesting that MP systems using Th require further investigation.

Overall, this work confirms that MP using DMF is a robust technique for plating Pu and Am, provides experimentally validated predictions of recoil efficiencies, determines recoil rates for ^{235m}U and ^{236}U, and identifies optimal source design parameters that link film thickness and morphology, substrate, and recoil output. These results provide a solid foundation for future precision spectroscopy experiments on ^{235m}U using recoil-ion sources and related systems.

Beyond the optimisation of Pu recoil-ion sources, this work establishes a general methodology for recoil-ion source development. By integrating complementary radiographic imaging, microscopy, spectroscopy and experimentally validated recoil transport simulations, the approach provides a transferable framework for linking thin-film properties to recoil-ion source performance. This methodology is expected to be applicable to the development of high-performance recoil-ion sources based on other α-emitting nuclides

Supplementary Information The online version contains supplementary material available at https://doi.org/10.1007/s10967-026-11025-5.

Acknowledgements The authors thank the staff of the workshops at JGU TRIGA and JYU for their support and advice for this project. The authors acknowledge support from the FORTHEM Alliance short-term mobility award, which funded the corresponding author's research visits to JYU. This project has received funding from the European Union Horizon 2020 Research and Innovation Programme under grant agreement number 861198, project 'LISA' (Laser Ionisation and Spectroscopy of Actinides), Marie Sklodowska-Curie Innovative Training Network (ITN).

Author contribution L.E.R. performed the majority of the experimental work, data analysis, simulations, and manuscript preparation. J.J., M.K., M.L., and T.S. arranged, conducted, and analysed the RBS measurements. A.T.L.B., C.M., D.R., J.R., and C.Z. assisted with source preparation, alpha measurements, and recoil collection. J.V. developed the software used for peak fitting and the decomposition procedure used for the alpha-measurement analysis. I.D.M., A.R., and J.W. arranged and conducted the unspiked-source alpha and gamma measurements, with L.E.R. assisting the measurements and performing the subsequent analysis. M.B., C.E.D., J.J., A.T.L.B., C.M., I.D.M., D.R., and J.V. contributed to manuscript review and discussion. All authors approved the final version and accepted responsibility for its content.

Funding Open Access funding enabled and organized by Projekt DEAL.

Data availability The data supporting the findings of this study are available within the paper and its Supplementary Information. Additional data are available from the corresponding author, L.E.R., upon reasonable request.

Declarations

Conflict of interest The authors declare no competing interests.

Declaration of of generative AI and AI-assisted technologies in the writing process During the preparation of this work, the authors used [ChatGPT 5.2] to improve readability and language. After using this tool, the authors reviewed and edited the content as needed and take full responsibility for the content of the published article.

References

1. Reed LE, Renisch D, Düllmann CE (2023) DICE: Apparatus for detection of internal conversion electrons. EPJ Web Conf 285:01002
2. Elwell R, Schneider C, Jeet J et al (2024) Laser excitation of the ^{229}Th nuclear isomeric transition in a solid-state host. Phys Rev Lett 133:013201
3. Ponce F, Swanberg E, Burke J et al (2018) Accurate measurement of the first excited nuclear state in ^{235}U. Phys Rev C 97:054310
4. Browne E, Tuli JK (2014) Nuclear data sheets for $A = 235$. Nucl Data Sheets 122:205–292
5. von der Wense L, Seiferle B (2020) The ^{229}Th isomer: prospects for a nuclear optical clock. Eur Phys J A 56:277
6. Shigekawa Y, Sawamura K, Hashiba S, et al (2026) Chemical effects on nuclear decay of ^{235}U isomer in the uranyl form. arXiv: 2603.01699. https://arxiv.org/abs/2603.01699. Accessed 8 Apr 2026
7. Shigekawa Y, Kasamatsu Y, Yasuda Y, Kaneko M, Watanabe M, Shinohara A (2018) Variation of half-life and internal-conversion electron energy spectrum between ^{235m}U oxide and fluoride. Phys Rev C 5(98):014306
8. Neve de Mevergnies M, Del Marmol P (1974) Effect of the oxidation state on the half-life of ^{235m}U. Phys Lett B 49:428–430
9. Neve de Mevergnies M (1972) Perturbation of the ^{235m}U Decay Date by Implantation in Transition Metals. Phys Rev Lett 29:1188–1191
10. Panov AD (1997) Quantitative conversion spectroscopy of the ultrasoft isomeric transition of uranium-235 and the electronic structure of uranium oxides. J Exp Theor Phys 85:313–324
11. Zhudov VI, Zelenkov AG, Kulakov VM et al (1979) Differential spectrum of the conversion electrons and the excitation energy of (1/2+)-uranium-235 isomer. JETP Lett 30:516–519
12. Parker W, Falk R (1962) Molecular plating: A method for the electrolytic formation of thin inorganic films. Nucl Instrum Meth 16:355–357
13. Zhu S (2022) Nuclear data sheets for $A = 236$. Nucl Data Sheets 182:2–129
14. Vascon A, Wiehl N, Reich T et al (2013) The performance of thin layers produced by molecular plating as α-particle sources. Nucl Instrum Methods Phys Res A 721:35–44
15. Vascon A, Santi S, Isse AA et al (2013) Smooth crack-free targets for nuclear applications produced by molecular plating. Nucl Instrum Meth Phys Res A 714:163–175
16. Vascon A, Santi S, Isse AA et al (2012) Elucidation of constant current density molecular plating. Nucl Instrum Methods Phys Res A 696:180–191
17. Artes E, Cavallo P, Häger T et al (2025) Influence of carbon dioxide and water concentration on terbium thin films produced by Molecular Plating. Radiochim Acta 113:779–789
18. Singh B, Tuli JK, Browne E (2022) Nuclear Structure and Decay Data for A=231 isobars. Nucl Data Sheets 185:560–830
19. Singh S, Singh B (2015) Nuclear Data Sheets for $A = 224$. Nucl Data Sheets 130:127–182
20. Browne E, Tuli JK (2011) Nuclear Data Sheets for $A = 220$. Nucl Data Sheets 112:1115–1161
21. Shigekawa Y, Kasamatsu Y, Shinohara A (2016) Developments and evaluation of a collection apparatus for recoil products for study of the deexcitation process of ^{235m}U. Rev Sci Instrum 87(5):053508
22. Allison J, Amako K, Apostolakis J et al (2016) Recent developments in Geant4. Nucl Instrum Meth Phys Res A 835:186–225
23. Allison J, Amako K, Apostolakis J et al (2006) Geant4 developments and applications. IEEE Trans Nucl Sci 53:270–278
24. Agostinelli S, Allison J, Amako K et al (2003) Geant4—a simulation toolkit. Nucl Instrum Methods Phys Res A 506:250–303
25. Reed LE, Düllmann CE, Loria Basto AT, et al (2026) Characterisation of Recoil Collection Efficiency and Precision Half-Life Measurements of ^{235m}U. In preparation
26. Klemenčič H, Benedik L (2010) Alpha-spectrometric thin source preparation with emphasis on homogeneity. Appl Radiat Isot 68:1247–1251

27. Trautmann N, Folger H (1989) Preparation of actinide targets by electrodeposition. Nucl Instrum Methods Phys Res A 282:102–106
28. Bond E, Moody WA, Dry DE et al (2013) Factors affecting the quality of plutonium deposits by electrodeposition. J Radioanal Nucl Chem 296:793–798
29. Bortels G, Collaers (1987) Analytical function for fitting peaks in alpha-particle spectra from Si detectors. Appl Radiat Isot 38:831–837. https://doi.org/10.1016/0883-2889(87)90180-8
30. Pommé S, Caro Marroyo B (2015) Improved peak shape fitting in alpha spectra. Appl Radiat Isot 96:148–153
31. Bé M-M, Chisté V, Dulieu C et al (2010) Table of radionuclides (Vol. 5 - A = 22 to 244). Bureau International des Poids et Mesures, Sèvres
32. Basunia MS (2006) Nuclear Data Sheets for $A = 237$. Nucl Data Sheets 107:2323–2422
33. Meyer C-C, Artes E, Bender M et al (2025) Microscopic and spectroscopic analysis of ion-irradiated molecular-plated thin films for superheavy element production. Nucl Instrum Meth Phys Res A 1075:170361
34. Artes E, Ackermann D, Düllmann CE et al (2025) Preparation of lanthanide thin films for ion beam experiments and post irradiation characterization. Nucl Instrum Meth Phys Res A 1075:170403
35. Pabst A (1933) Crystallography of some compounds of gadolinium and samarium. American J Sci 5(151):72–79
36. Nicholas AD, Arteaga A, Ducati LC et al (2023) Insight into the Structural and Emissive Behavior of a Three-Dimensional Americium(III) Formate Coordination Polymer. Chem Eur J 29:202300077
37. Henrie J, Kellis S, Schultz SM et al (2004) Electronic color charts for dielectric films on silicon. Opt Express 12:1464–1469
38. Pugmire DL, Freibert FJ, Baiardo JP (2013) The optical properties of the plutonium/plutonium oxide thin film system. Actin Res Q 2:47–50
39. Scriven L, Sternling C (1960) The Marangoni Effects. Nature 187:186–188
40. Kaiser N (2002) Review of the fundamentals of thin-film growth. Appl Opt 41:3053–3060
41. Eren B, Marot L, Günzburger G et al (2014) Hydrogen-induced buckling of gold films. J Phys D Appl Phys 47:025302
42. Jain RK, Jain A, Agarwal G et al (2007) Electrical and optical properties of hydrogenated RNi_5 / Co (R = Ce, La) bi-layer systems. Int J Hydrogen Energy 32:1916–1921
43. Morisset A, Cabal R, Grange B et al (2019) Highly passivating and blister-free hole selective poly-silicon based contact for large area crystalline silicon solar cells. Sol Eng Mater Sol Cells 200:109912
44. Kuznetsov AS, Gleeson MA, Bijkerk F (2014) Temperature dependencies of hydrogen-induced blistering of thin film multilayers. J Appl Phys 115:173510
45. Dai Y, Odette GR, Yamamoto T (2012). In: Konings RJM (ed) Comprehensive Nuclear Materials. Elsevier, Amsterdam
46. Iwakiri H, Yasunaga K, Morishita K, Yoshida N (2000) Microstructure evolution in tungsten during low-energy helium ion irradiation. J Nucl Mater 283–287:1134–1138
47. Berkelaar RP, Bampoulis P, Dietrich E et al (2015) Water-Induced Blister Formation in a Thin Film Polymer. Langmuir 31:1017–1025
48. Aleksandrov PA, Baranova EK, Baranova IV et al (2003) Behavior of implanted hydrogen in thermally stimulated blistering in silicon. Radiat Eff Defects Solids 158:771–781
49. Li T, Dai X, Su J et al (2026) Hydrogen plasma-induced blistering on aluminum: morphology, growth, and interfacial energetics. Scripta Mater 272:117055
50. Tiegel MC, Martin ML, Lehmberg AK et al (2016) Crack and blister initiation and growth in purified iron due to hydrogen loading. Acta Mater 115:24–34
51. Browne E (2006) Nuclear Data Sheets for for $A = 232$. Nucl Data Sheets 107:2579–2648
52. Nesaraja CD (2023) Nuclear Data Sheets for $A = 245$. Nucl Data Sheets 189:1–110
53. Schuman RP, Tromp RL (1959) Calculation of the composition of reactor-irradiated heavy nuclides. IDO-16571. Phillips Petroleum Co., Atomic Energy Division, U.S. Atomic Energy Commission
54. Runke J, Düllmann CE, Eberhardt K et al (2014) Preparation of actinide targets for the synthesis of the heaviest elements. J Radioanal Nucl Chem 299:1081–1084
55. Julin J (2025) JaBS (version 0.7.6). https://doi.org/10.5281/zenodo.6362701
56. Lazarus V, Pauchard L (2011) From craquelures to spiral crack patterns: Influence of layer thickness on the crack patterns induced by desiccation. Soft Matter 7:2552–2559
57. Osman A, Goehring L, Stitt H et al (2020) Controlling the drying-induced peeling of colloidal films. Soft Matter 16:8345–8351
58. Lee WP, Routh AF (2004) Why do drying films crack? Langmuir 20:9885–9888
59. Liu T, Luo H, Ma J et al (2014) Tuning crack pattern by phase separation in the drying of binary colloid-polymer suspension. Phys Lett A 378:1191–1199